Low velocity streaks combined with intrinsic flame instabilities provoke boundary layer flashback in a turbulent premixed jet-stabilized hydrogen flame

Porath, P.; Altenburg, L. A.; Klein, S. A.; Tummers, M. J.; Ghani, A.

DOI
10.1016/j.combustflame.2025.114236

Publication date
2025

Document Version
Final published version

Published in
Combustion and Flame

Combustion and Flame 278 (2025) 114236

Contents lists available at ScienceDirect

Combustion and Flame

journal homepage: www.sciencedirect.com/journal/combustion-and-flame

Low velocity streaks combined with intrinsic flame instabilities provoke boundary layer flashback in a turbulent premixed jet-stabilized hydrogen flame

P. Porath [a,*], L.A. Altenburg [b], S.A. Klein [b], M.J. Tummers [b], A. Ghani [a,c]

[a] Data Analysis and Modeling of Turbulent Flows, Technische Universität Berlin, Müller-Breslau-Straße 15, 10623 Berlin, Germany
[b] Department of Process and Energy, Delft University of Technology, Mekelweg 2, 2628 CD Delft, The Netherlands
[c] Institute for Reactive Flows, Leibniz University Hannover, An der Universität 1, 30823 Garbsen, Germany

ARTICLE INFO

Keywords:
Hydrogen flame
Boundary layer flashback
Turbulent premixed combustion

ABSTRACT

We report on boundary layer flashback of a turbulent premixed, pure hydrogen flame using well-resolved LES. This numerical work is based on flashback experiments of the TU Delft (TUD) jet flame at a jet Reynolds number of $Re = 11000$. Flashback is a highly sensitive process, which is why (i) the turbulent inflow conditions, (ii) chemistry modeling and (iii) the wall temperatures of the mixing tube are crucial parameters to predict accurately this transient process. The presence of thermo-diffusive flame instabilities is the main contributor for flashback in this setup. We identify quasi-coherent turbulent structures in the mixing tube, namely an ejection event, which transports slow, preheated and hydrogen-enriched fluid away from the wall and triggers the flashback event. As a result, the flame forms a convex cusp upstream of the tube exit pointing towards the unburnt gas mixture. During the transition from unconfined (no walls around the flame) to confined (flame surrounded by walls) boundary-layer flashback, this cusp further bends and propagates towards the jet exit center, while, at the same time, its curvature and the reaction rate of hydrogen significantly increase by a factor of two. We repeated the flashback simulations several times and also for various flow conditions: all cases feature the same FB characteristics and, hence, confirms the generality of the conclusions. Moreover, the numerical flashback mechanism confirms the process hypothesized by the experiments. Based on the identified governing key parameters that affect flame flashback, we performed parametric variations of the Lewis number and wall temperature. By varying the Lewis number, we can clearly state that the flashback is driven by thermo-diffusive instabilities, while a hotter wall significantly deteriorates the flashback behavior of this setup.

Novelty and significance statement

Hydrogen combustion plays a crucial role in various energy applications due to no CO_2 emissions. However, lean premixed hydrogen/air combustion can lead to safety challenges, particularly in the form of flame flashback, potentially causing catastrophic failures in combustion chambers. Understanding and controlling flashback is essential to ensure the safe and efficient use of hydrogen for instance in gas turbines. With this study, we address a number of open questions:

(i) root cause of boundary layer flashback in turbulent premixed lean 100% hydrogen jet flames.
(ii) transition from unconfined to confined boundary layer flashback.
(iii) investigate key parameters that govern flame flashback: Lewis number and wall temperature.

This study demonstrates for the first time that flashback in turbulent premixed lean hydrogen combustion is driven by the characteristic behavior of thermo-diffusive instabilities.

1. Introduction

Hydrogen is a carbon-free and sustainable fuel that shows great potential to mitigate greenhouse gases. For this reason, the combustion community seeks new burner technologies that can reliably run on 100% hydrogen [1]. At the same time, the application of hydrogen in premixed combustion systems involves major concerns, such as flame flashback (FB), where the flame propagates upstream into the mixing tube. This is mainly because of the particular characteristics

* Corresponding author.
E-mail address: porath@tu-berlin.de (P. Porath).

https://doi.org/10.1016/j.combustflame.2025.114236
Received 4 December 2024; Received in revised form 8 May 2025; Accepted 10 May 2025
Available online 4 June 2025

Nomenclature

Latin

A_0	Averaged flame surface
BL	Boundary layer
CFL	Courant–Friedrichs–Lewy
CHT	Conjugate heat transfer
c	Progress variable
c_p	Isobaric specific heat capacity
D	Mixing tube diameter
D_m	Mass diffusion coefficient
D_t	Thermal diffusion coefficient
DNS	Direct numerical simulation
FB	Flashback
FLF	Flame leading finger
FLP	Flame leading point
f	Body force/forcing
H	Enthalpy
H_2	Hydrogen
HOQ	Head-on quenching
HR	Heat release
I_0	Stretch factor
Le	Lewis number
LVS	Low velocity streak
Ma	Mach number
N	Number of
p	Pressure
PIV	Particle Image Velocimetry
Pr	Prandtl number
q	Enthalpy flux
R	Specific gas constant
Re	Reynolds number
Sc	Schmidt number
SWQ	Side-wall quenching
t	Time
T	Temperature
TC	Thermocouple
TDI	Thermo-diffusive instability
TUD	TU Delft
u	Velocity
u_b	Bulk velocity
V_c	Correction velocity
WALE	Wall adapting local eddy-viscosity
Y	Mass fraction
Z	Mixture fraction

Greek

$\boldsymbol{\Delta}$	Cell size
λ	Thermal conductivity
ν	Stoichiometric coefficient
ρ	Density
$\boldsymbol{\Phi}$	Equivalence ratio
ω	Production rate

Subscripts

$(\cdot)_r$	Radial
$(\cdot)_x$	Streamwise
$(\cdot)_t$	Turbulent
$(\cdot)_0$	Unburnt

Superscripts

$\widetilde{(\cdot)}$	Filtered quantities
$(\cdot)'$	Remaining fluctuation
$\overline{(\cdot)}$	Temporal mean
$(\cdot)^S$	Soret effect

of hydrogen flames [2]. Due to the increased flame speeds and in some cases significantly reduced flame thicknesses, premixed hydrogen combustion is particularly prone to FB in regions with low flow velocities, which is mainly in the boundary layer (BL). Here, the flashback mechanisms refers to boundary layer flashback (BLF). It is highly important to understand the leading mechanisms of BLF in order to further apply hydrogen in technical devices.

Non-swirled BLF has been investigated experimentally [3–7] and numerically [8–10]. For confined, where the flame is surrounded by walls, both swirled and non-swirled flames, DNS and LES have been carried out for mostly canonical channel burners [8–12]. In these numerical cases, the flame is already in a confined state, not including the transitional behavior of the flame from a unconfined to a confined state. Except for only one LES study (to the best knowledge of the authors) on the transition from unconfined to confined BLF in turbulent premixed hydrogen combustion in tube burners, which has been performed by Endres [9]. In his case, FB is obtained by an increase of the fuel mass flow at constant bulk velocity. The FB event directly occurs at the burner rim with a low velocity region as the triggering event. Similar observations are made experimentally by Eichler et al. [3] and Baumgartner et al. [5]. The former studied the difference in FB propensity between a confined and unconfined geometry showing the relevance of confined geometries, while the latter investigated the transition from an unconfined to a confined configuration in a channel burner setup. However, there is no detailed numerical analysis of the transition from an unconfined to a confined FB. But, more importantly, several experimental studies at atmospheric conditions reveal the significant increase in FB propensity using solely hydrogen as the fuel, indicating a different burning behavior compared to natural gas combustion [3,6]. As stated by Kalantari [13], there is a lack of numerical simulations in capturing the detailed effects of FB at 100% hydrogen in jet flames since the underlying characteristics are not yet well understood. With this study, we contribute towards this gap and provide a numerical framework based on well resolved LES in terms of both wall and flame, which is able to (i) capture 100% H_2 FB and (ii) explain the transition from unconfined to confined FB. Here, the flame region is resolved similarly to a DNS, while the remaining domain is treated as a LES. This is an appropriate approach to analyze flashback and to perform parametric studies.

It is challenging to simulate hydrogen combustion with high-fidelity, which is seen from the spare amount of numerical studies on turbulent hydrogen/air combustion that go beyond canonical DNS setups to rather realistic applications. Hydrogen modeling is especially challenging due to the potential occurrence of intrinsic flame instabilities, namely thermo-diffusive instabilities (TDIs). This is because the computational cost increases significantly. Driven by Lewis numbers significantly smaller than unity, molecular diffusion of hydrogen is faster than the heat diffusion, which triggers the cellular structures in lean H_2/air mixtures [14]. As shown in numerous DNS studies of canonical flames, TDIs increase burning rates, and thus, the flame speeds increase in convexly formed flame fingers pointing towards the unburnt mixture. Up to now, no numerical study describes the transient BLF process in a jet flame configuration and demonstrates that the FB

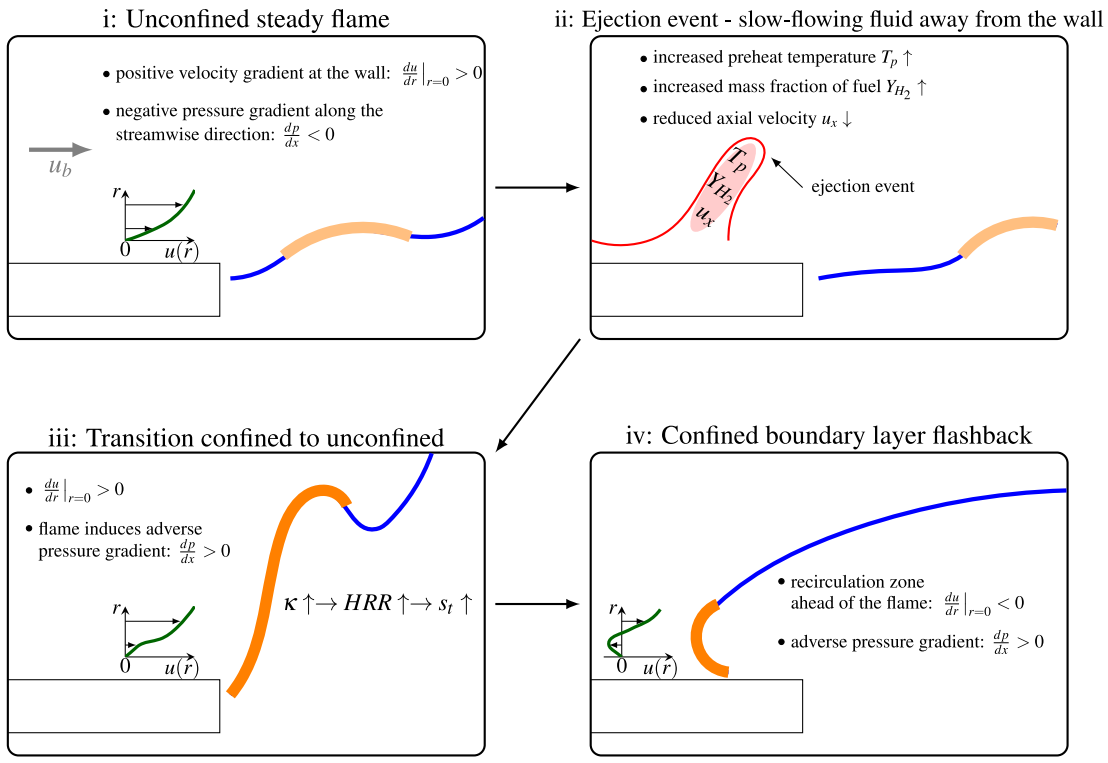

Fig. 1. Boundary layer flashback process: undisturbed flame with moderately burning rates indicated by light orange line (i). Occurrence of an ejection event, which transports slow flowing, preheated and H_2-enriched fluid away from the wall (ii). The flame reacts to the ejection event by increased burning rates (dark orange) (iii), which eventually leads to flame flashback in the boundary layer. Thereafter, the flame is confined by the tube wall, and thus, the upstream flame propagation accelerates (iv).

mechanism is TDI-driven. For that, we choose a hybrid approach, where the flame region close to the walls are fully resolved (flame-resolved DNS), while the remaining domain, which is of non-reacting nature, is modeled via LES.

The Soret effect, which accounts for thermal diffusion (e.g. light hydrogen molecules diffuse along a temperature gradient towards a heated wall) must be considered in FB studies. Only recently, Fruzza et al. showed the importance of the Soret effect in predicting flashback limits using laminar domestic burners [15]. Apart from the Soret effect consideration, Duan et al. identified the wall temperature as a key contributor to flashback [16]: the higher the wall temperature, the higher the FB propensity. The interaction between the flame and the wall can influence the local flow field, heat transfer, and chemical reactions [17,18]. When the flame is close to the wall, the heat loss to the wall can quench the flame or alter its structure [19,20]. Understanding these interactions is essential for designing combustion systems that minimize the risk of flashback, ensuring safe and efficient operation.

We distinguish our findings of the main characteristics during FB by four phases (Fig. 1), which starts with an unconfined steadily burning flame (i). A low velocity streak occurs in the tube flow close to the walls. This behavior is well known from wall bounded pipe flows [21–23]: An ejection event, which is further enhanced by combustion as stated by Chen et al. [10], transports slow-flowing, pre-heated and hydrogen enriched fluid from the wall to the core flow (ii). The flame then responds to the ejection event with the formation of an elongated flame finger (iii). The flame finger significantly increases the typical features of turbulent premixed hydrogen combustion, e.g. the flame is more curved towards the unburnt mixture, which leads to higher reaction rates and an increased turbulent consumption speed (iii) (detailed in Section 6.3). Moreover, the flame finger also causes a positive pressure gradient in the BL, which additionally de-accelerates the incoming flow profile and, hence, provokes FB. These characteristics combined cause the flame to move upstream into the mixing tube, where the upstream propagation is intensified by the formation of a recirculation zone ahead of the leading flame point (iv).

The paper is structured as follows: Section 2 describes the target configuration, followed by Section 3, where the numerical methodology is presented. Subsequently, both the non-reactive and the reactive flow field are compared to the experimental data in Sections 4.1 and 4.2, respectively. The following sections are based on Fig. 1: Section 5 describes the steady H_2 flame characteristics (i), while a detailed analysis of the flashback process is found in Section 6 (ii–iv). Finally, both the impact of the unity Lewis number and the impact of the increased wall temperature on FB behavior are analyzed in Sections 7.1 and 7.2, respectively.

2. Target configuration

2.1. Experimental setup

The flame flashback experiments at the TU Delft (TUD) burner are performed with a Bunsen burner at ambient pressure [24]. The burner assembly consists of a horizontal and a vertical mixing tube with a length of $l_h = 1.45\,\text{m}$ and $l_v = 1.25\,\text{m}$, respectively, that are connected by a 90° turn (Fig. 2). Both pipes have an inner diameter D and a wall thickness t_{wall}. Hydrogen and (seeded) air are injected upstream into the mixing tube to realize a uniform mixture at the burner exit. The mean velocity and the Reynolds stress profiles that are measured at the pipe exit are consistent with a fully developed turbulent pipe flow [25]. Different burner tubes and different flames are considered in the experimental campaigns at the TUD (Table 1). In all cases the unburnt mixture temperature is $T_p = 295\,\text{K}$. The burner tube is not thermally controlled in the sense that it is not actively cooled. Several thermocouples monitor the burner temperature during the burner operation. These are attached to the outer wall of the burner tube at different axial positions. The closest position to the burner rim is at a distance of $x = 2\,\text{mm}$ (Fig. 2).

Particle Image Velocimetry (PIV) is used to measure the velocity field in a planar cross section of the flow. The PIV system uses a

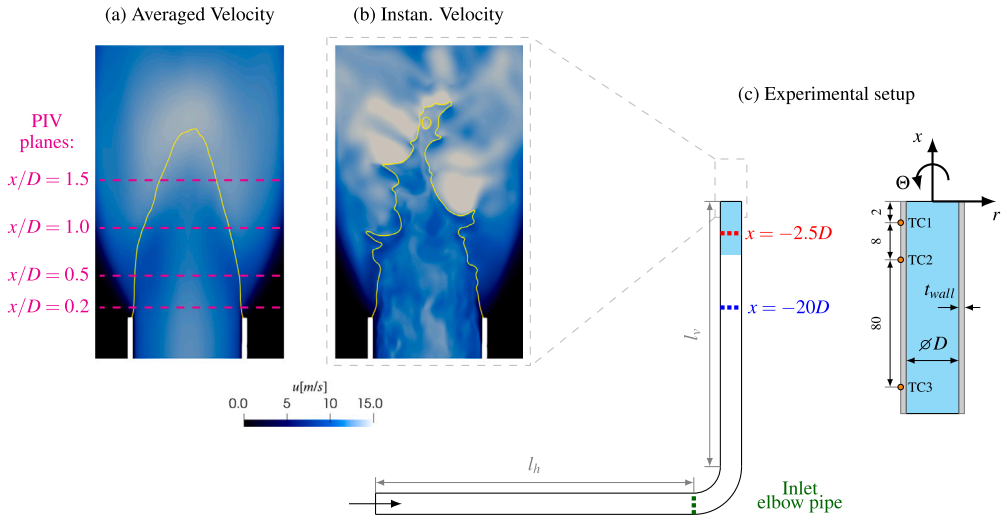

Fig. 2. Sketch of the Bunsen burner used at TUD (c). PIV data is extracted at the magenta lines (a), while the red and blue dotted lines correspond to the inlet of the short and long numerical domain (c), respectively. Averaged (a) and instantaneous (b) velocity fields from the LES are depicted.

Table 1
The two cases considered in this study.

Case	Tube inner diameter D [mm]	Tube wall thickness t_{wall} [mm]	Tube material	Equivalence ratio Φ	Reynolds number Re
A	20.1	1.0	Copper	0.6	11 000
B	25.2	1.5	Quartz	0.49	12 500

Quantronix Darwin Duo Pro 52780M laser that emits a beam of green light at a wavelength of 527 nm. The laser beam is converted into an approximately 1 mm thick light sheet by a series of lenses. The hydrogen-air mixture is seeded with aluminium-oxide particles with a mean diameter of 1 µm. The images of the seeding particles are recorded by a Photron Fastcam SA1.1 camera. The images were processed with DaVis 8.4.0 using multi-pass iterations with decreasing interrogation window size, i.e., one pass was made with a window size of 32 × 32 pixels and an overlap of 50% and then three passes were made with a window size of 16 × 16 pixels and an overlap of 75%.

2.2. Flashback in the experiments: triggering and mechanism

Flashback is initialized as follows: the fresh gas bulk velocity u_b is gradually decreased in small steps, while the mixture composition remains unchanged. Note that thermal equilibrium is maintained after each reduction in velocity. The entire process, starting from a stable operating point to the flame upstream propagation, takes several minutes. Each FB event was repeated three times to get an impression of the reproducibility. Once the flame jumps into the mixing tube, the corresponding wall temperature T_w and bulk velocity u_b are registered. For case A the resulting values are $T_w = 346$ K and $u_b = 9.6$ m/s. As stated by Faldella, the stochastic scatter of the FB events for a single operating point in case A is fairly large [26]: although thermal equilibrium is always considered in the experiments and thus, remained at a single operation point for a relative long time, the standard deviation within the bounds of the measured bulk velocities at $\Phi = 0.6$ is approximately $\sigma = 0.55$ m/s. Knowing that the lower bound of the flashback occurrence in the experiments is $u_b = 9.0$ m/s, we use this value as a reference for evaluating the numerical accuracy. Regarding the measured wall temperature: it is very unlikely that the position of the thermocouple coincides with the position where the flame enters the mixing tube. Thus, the exact wall temperature during FB is difficult to determine in the experiments.

In a similar setup to case B ($\phi = 0.4$ instead of $\phi = 0.49$), the BLF is characterized by PIV measurement data (Fig. 3). Clearly, the FB is triggered by a low velocity streak, interacting with the flame (blue region in the mixing tube closer to the wall). This velocity perturbation causes a convex flame bulge, which then propagates upstream into the mixing tube. This is in line with the current understanding of BLF [13].

Flashback is initialized at a random position along the circumference of burner tube edge, which cannot be determined prior to the FB occurrence. Due to the highly stochastic behavior, matching the exact position of flame upstream propagation with the PIV measurement plane in the experiments is nearly impossible. PIV is a 2D velocity measurement technique. Even though the round jet is axisymmetric allowing to describe flow-related characteristics on a plane surface, there is no prior knowledge of the position where the flame enters the mixing tube. Meaning that the likelihood of the previously aligned (prior to the experiments) plane capturing the exact position of the flashback is small. Thus, numerical tools give better insight in the physical features of BLF by assessing the entire flow field.

3. Numerical methodology

The flashback event of the TUD burner is studied using an incompressible flow solver [27]. We choose a low-Mach solver to exclude possible acoustic pressure fluctuations to focus primarily on the acoustically undisturbed flame-flow interactions during the FB process to ensure that TDIs are the main FB driver. The conservation equations for reacting flows are solved using a finite volume method in the low-Mach regime (Ma = 0.0576). For the case investigated here, the maximum flow velocity occurring in the domain is $u = 20$ m/s. This is of importance because acoustic tones that lead to FB have been reported in Goldmann et al. in similar setup with high H_2-content. [6]. The change in density is evaluated from the equation of state at the thermodynamic pressure (reference pressure $p_{ref} = 1$ bar) and thus only depends on the temperature T:

$$\rho = \frac{p_{ref}}{RT}, \tag{1}$$

where R is the universal gas constant. Applying the filter operation $\bar{\cdot}$ to the conservation equations of reactive flows in the low Mach regime, the following set of LES equations are obtained:

$$\text{Mass} \quad \frac{\partial \bar{\rho}}{\partial t} + \frac{\partial \bar{\rho}\tilde{u}_i}{\partial x_i} = 0 \tag{2}$$

$$\text{Momentum} \quad \frac{\partial}{\partial t}\bar{\rho}\tilde{u}_j + \frac{\partial}{\partial x_i}\bar{\rho}\tilde{u}_i\tilde{u}_j + \frac{\partial \bar{p}}{\partial x_j} = \frac{\partial \bar{\tau}_{ij}}{\partial x_i} + \frac{\partial}{\partial x_i}\bar{\rho}\left(\tilde{u}_i\tilde{u}_j - \widetilde{u_i u_j}\right) \tag{3}$$

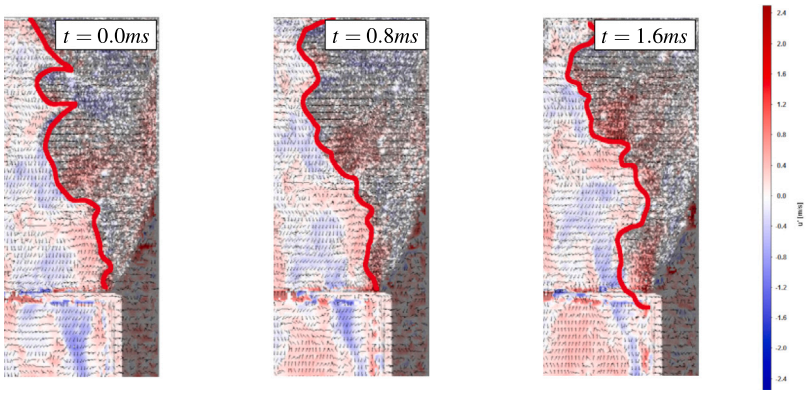

Fig. 3. Experimental PIV-data of BLF in the TUD setup. Axial velocity fluctuations are characterized by positive (red) and negative (blue) values. The flame is denoted by the red line.
Source: Adopted from [25].

$$\text{Species} \quad \frac{\partial \bar{\rho}\tilde{Y}_k}{\partial t} + \frac{\partial}{\partial x_i}\bar{\rho}\tilde{u}_i\tilde{Y}_k = -\frac{\partial}{\partial x_i}\left[-\bar{\rho}\left(\left(\bar{D}_{k,m} + \frac{\mu_t}{Sc_t}\right)\frac{\partial \tilde{Y}_k}{\partial x_i} + \frac{\bar{D}_{k,t}}{\bar{\rho}\tilde{T}}\frac{\partial \tilde{T}}{\partial x_i} - \tilde{Y}_k\tilde{V}_c\right)\right] + \bar{\dot{\omega}}_k \tag{4}$$

$$\text{Energy} \quad \frac{\partial \bar{\rho}\tilde{H}}{\partial t} + \frac{\partial}{\partial x_i}\bar{\rho}\tilde{u}_i\tilde{H} + \frac{\partial}{\partial x_i}\bar{\rho}\frac{\mu_t}{Pr_t}\frac{\partial \tilde{H}}{\partial x_i} = \bar{\dot{\omega}}_T + \frac{\partial \bar{p}}{\partial t} - \frac{\partial \bar{q}_i}{\partial x_i} \tag{5}$$

A second order implicit time integration scheme with an iterative predictor corrector scheme (SIMPLEC) is applied. The timestep is determined by the CFL number, which depends on local mesh size and velocity. It is ensured that the CFL number does not exceed 1.0. This results in a time step size of $\Delta t = 1$ µs.

The bounded-central differencing is selected as the discretization scheme of the convective fluxes in the Navier–Stokes equations, while both the species and energy equation use a second-order upwind scheme. For the diffusive fluxes a second-order expression is chosen.

The subgrid scale turbulent viscosity, which accounts for the effects of the small eddies on the resolved flow field, is described by the WALE model [28]. The interaction between the flame and turbulent structures is resolved by accounting for a sufficient number of points in the flame to capture the TDIs accurately. The reacting species transport equations are solved using the CVODE solver with the operator splitting algorithm [29].

The dynamic viscosity and thermal conductivity of the mixture are computed by Mathur-Saxena averaging [30]. The dynamic viscosity of each species is determined by the method of Chapman-Enskog [30]. This is a necessary step to enable differential diffusion. It is modeled using Fick's law: $J_i = -\rho D_{i,m}\nabla\tilde{Y}_i$, where $D_{i,m}$ is the molecular diffusivity of species i in the mixture. This coefficient is calculated from the ratio of the kinematic viscosity and the Schmidt numbers of each species in the burnt gas that are obtained from freely propagating, 1D, adiabatic Cantera simulations using detailed H_2-chemistry, namely the Burke mechanism. This results in a non-unity Lewis number approach. To ensure global mass conservation, a correction velocity $\tilde{V}_c$ is introduced in the species equation:

$$\tilde{V}_c = \sum_{k=1}^{N}\left(\left(\bar{D}_{k,m} + \frac{\mu_t}{Sc_t}\right)\frac{\partial \tilde{Y}_k}{\partial x_i} + \frac{\bar{D}_{k,t}}{\bar{\rho}\tilde{T}}\frac{\partial \tilde{T}}{\partial x_i}\right) \tag{6}$$

The molecular diffusive flux is complemented by the Soret effect, where the thermal diffusion coefficient $D_{i,t}$ is determined according to the Warnatz model [31]: $V^s_{k,i} = D_{i,t}/\tilde{T}\partial\tilde{T}/\partial x_j$.

3.1. Numerical domains and mesh requirements

We consider two fluid domains in our study, referring to a long and a short domain (Fig. 2). The long domain is truncated $20D$ upstream of the tube exit, whereas the short domain has a tube length of $L = 2.5D$, measured from the tube exit. First, we determine the flow characteristics of the long domain by imposing synthetic turbulence injection at the inlet [32]. Second, we check the short domain to produce similar inflow characteristics compared to the long domain. A constant velocity inlet profile ($u = u_{max}(1 - r/R)^{1/3}$) is used for the long domain, while time-resolved velocity profiles are extracted from the auxiliary (long) LES for the short domain (Section 3.2). Note that the short domain is tailored for reactive flow simulations to reduce both the cell number and the flow-through time. In both domains the outlet pressure boundary section is identical where a large geometry with a length of $80D$ and diameter of $40D$ is used (Fig. 4). In doing so, the large outlet section (i) mimics the experimental setup and (ii) eliminates the impact of the boundary condition on the flow field in the region of interest (flame). Since a turbulent jet entrains surrounding air, we introduce a coflow airflow inlet, which accounts for the entrained air and hence, injects air at atmospheric conditions ($p = 1\,\text{bar}, T = 300\,\text{K}$) with an uniform velocity of $u_{coflow} = 0.1\,\text{m/s}$. Note that there are no controlled boundary conditions for the surrounding air, since this jet flame burns in an atmospheric environment. In order to investigate the impact of the elbow pipe on the non-reacting flow characteristics, we extend the tube length covering the entire elbow pipe (Fig. 2, green line). Since the results remain unaltered by the extension (Fig. B.25 in the appendix), the long tube is not further considered throughout this study.

A semi-structured trimmed mesh with approximately 150M cells is used for the short domain (Fig. 4a). The mesh inside the mixing tube is uniform in the streamwise direction, while the resolution is coarsened from the wall ($\Delta x = 0.24$ mm) to the free stream ($\Delta x = 0.48$ mm). Downstream of the flame region, the mesh is successively coarsened to a maximum cell size of $\Delta x = 3.64$ mm prior to the pressure outlet. The wall boundary layer is well resolved by realizing y^+ values below unity everywhere in the short tube (Fig. 4b). The flame region in the vicinity of the wall, where the boundary layer flashback takes place, is resolved by 12 points in the flame front ($\Delta x = 0.03$ mm), while away from the wall six points describe the flame movement ($\Delta x = 0.06$ mm). Note that the flame resolution refers to a one-dimensional, premixed and unstretched flame, evaluated at the operating condition of the configuration. The flame thickness is computed by $\delta_f = \left(T_b - T_u/max\right)\left(\left|\frac{\partial T}{\partial x}\right|\right)$ using the Burke mechanism in a 1D adiabatic flame using Cantera. Thermo-diffusive instabilities depend on the flame resolution [33,34] and an accurate prediction relies on the grid resolution. Since we aim to capture flashback and the transition from an unconfined to a confined configuration, the exit area in the tube has the same resolution as the flame ($\Delta x = 0.03$ mm).

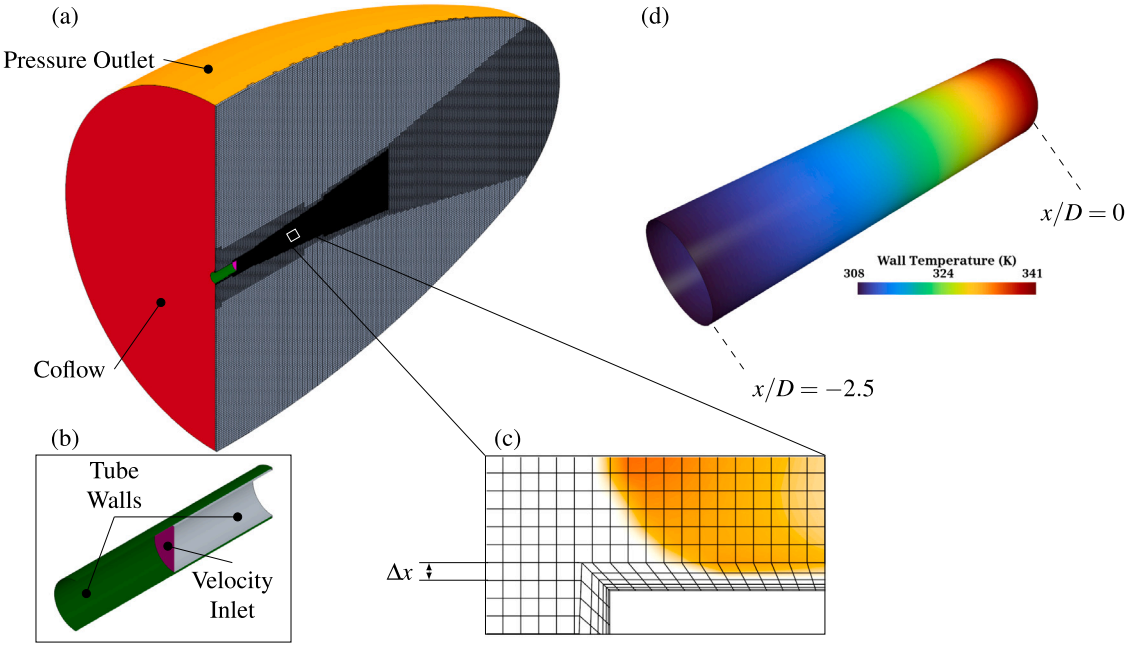

Fig. 4. 2.5D Domain with mesh size on the middle cut plane (a). Zoomed view of the mixing tube (b). Heat release distribution indicates the flame position close to the wall and the required grid resolution to resolve the near-wall flow (c). Wall temperature distribution is obtained from additional CHT computations (d).

Based on the numerical setup, we approach flame flashback using a flame-resolved DNS, while other effects such as entrainment are modeled on a LES-type of grid resolution. This strategy saves a significant amount of computational time so that parametric studies can be performed as shown later. To highlight the difference between DNS and LES, a small ratio between turbulent and laminar viscosity is realized, indicating a flame-resolved DNS in the important region for flame flashback (Fig. A.24 in the appendix).

As in the experiments, flame flashback in the LES is triggered by reducing the flow velocity steadily. Due to high computational cost, it is infeasible to mimic the ramp in the experiments because this would require compute times of several minutes. The ramp in the LES is significantly shorter than in the experiments, which limits the stochastic behavior of the flashback event.

3.2. Validation of turbulent inflow conditions

Matching the turbulent inflow conditions is an essential step in not only capture the turbulent flow characteristics in the numerical domain, but also in modeling flame flashback. Hence, we examine the short ($x = 2.5D$) and the long domain ($x = 20D$) for the capability of matching cold flow characteristics (only air without combustion) recorded experimentally. While doing so, the mean axial velocity profiles as well as the Reynolds stresses in axial and radial direction are analyzed at various axial planes downstream of the jet exit. The positions of the planes are indicated in Fig. 2. The cold flow velocity profiles at $x = 2.5D$ are eventually fed into the reactive LES as inlet conditions. The results are shown in Section 4.

3.3. Chemistry modeling

The chemical reactions are solved with finite rate chemistry using the Burke mechanism that contains 9 species and 27 reactions [35]. The Cantera simulation of 1D flames with a detailed reaction mechanism (Burke) for hydrogen/air combustion at condition of the experiment is performed. Next, the profiles are compared to the solver results using the Burke mechanism in a 1D flame identical to Cantera (Fig. 5). Our numerical setup predicts very similar profiles as the chemical kinetics solver Cantera. This step is necessary to evaluate the performance of the reduced mechanism implemented in the solver. The latter captures the profiles (u, T, heat release (HR), major and minor species) of the detailed mechanism correctly.

3.4. Wall temperature

For two main reasons the wall temperature must be set correctly to capture BLF. First, a hot wall heats up the surrounding fresh gas mixture, which, in turn, increases e.g. the local flame speed. Second, hydrogen is a light molecule, which will diffuse along a temperature gradient towards the wall, leading to locally higher mass fraction values. We determine the wall temperature by performing a weakly coupled CHT simulation, where the fluid and solid domains are solved with different time scales in a sequential manner [36,37]. The wall temperature distribution is obtained from a steady-state simulation at a constant bulk velocity close to the FB condition. The resulting wall temperature profile along the mixing tube is imposed as a steady temperature profile for the transient FB process. By doing so, we assume that FB occurs at a much smaller time scale than the heat up of the wall (thermal inertia). Again, this is a simplification compared to the experiments (see Section 2), but ensures a more precise comparison and separation of flow effects for different wall temperatures (Section 7.2).

Due to the high thermal conductivity of copper, the tube walls will heat up less than conventional burner materials (such as steel). According to the experiments, a burner tip temperature of $T = 346\,\mathrm{K}$ is observed at one specific point during FB. The flame generates heat which is conducted through the fluid into the solid, resulting in an increase in the solid material above the atmospheric temperature ($T_w > 300\,\mathrm{K}$). From there, the heat is transported through the solid by conduction, causing the increased observed wall temperature at the outer wall surface. The CHT simulations predict a slightly lower value ($T = 341\,\mathrm{K}$) than observed in the experiments (Fig. 4b). The relative error between the predicted and actual value is 1.2%. We use this wall temperature for the FB analysis in the next sections. Note that only one single thermocouple measures the wall temperature at the burner rim which does not necessarily coincide with the position of the onset of the flame flashback. Thus, the position at which the wall temperature during the FB event is measured, might be lower than the actual temperature of the wall, where the flame is present.

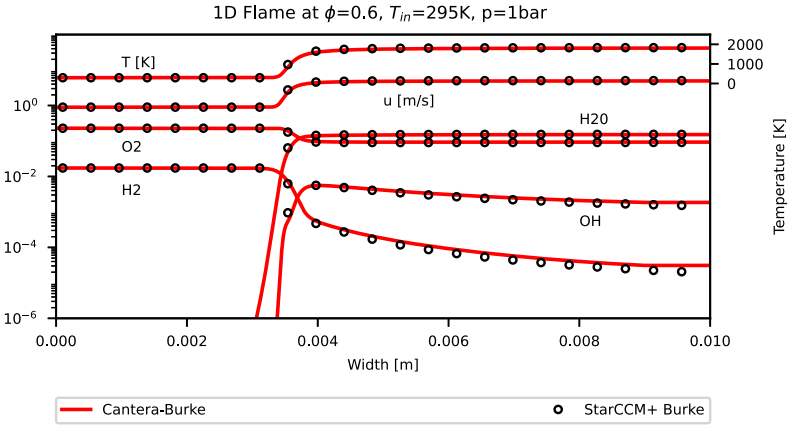

Fig. 5. Simulations of 1D laminar, premixed, adiabatic freely propagating hydrogen-air flames for a given operation point using Cantera and incompressible low Mach flow solver. Red solid lines represent a detailed reaction mechanism (Burke) in Cantera, while the flow solver is indicated by the black dots. StarCCM+ with the Burke mechanism is capable of capturing the reactive flow properties such as laminar flame speed which is a key parameter in predicting flame flashback.

Table 2
Wall temperature at the flashback occurrence and material properties of the copper and quartz tube.

Case	T_w [K]	λ [W/m K]	ρ [kg/m^3]	c_p [J/kg K]
A (copper)	346 ($x = -2$ mm)	398	8940	386
B (quartz)	333 ($x = -10$ mm)	1.4	2500	840

4. Validation of the non-reacting and reacting flow field

Both the non-reacting and the reacting flow field of the LES are validated against experimental PIV data from case B using the quartz tube with a Reynolds number of $Re = 12\,500$ (Table 1). Unlike the setup of the copper tube, the quartz tube differs in three major points: (i) inner diameter $D = 25$ mm, (ii) burner material and (iii) the equivalence ratio which is set to $\Phi = 0.49$ instead of $\Phi = 0.6$ for the reacting case. We decide to use this configuration as validation for our numerical framework (case B), while using the copper tube for FB considerations (case A). In the copper case, the maximum wall temperature is below $T = 350$ K. Table 2 contains the wall temperature measured during the flashback occurrence and the material properties of quartz and copper. Note that the position of the thermocouple in the quartz tube configuration is placed 8 mm further upstream due to the high wall temperatures at the burner rim, which are caused by the low thermal conductivity of quartz compared to copper.

4.1. Coldflow results

For validation purposes, we consider the mean axial velocity profiles (first row), the axial Reynolds stresses (second row) and Reynolds shear stresses (third row) at four representative axial positions (columns) (Fig. 6). The mean axial velocity profile from the experiments (squares) at each axial position is correctly reproduced by the LES. Moreover, the jet widening, which is caused by the entrainment air, is captured sufficiently. There are hardly any differences between the short (solid blue line) and long (dotted red line) domain in the axial velocity profile. The same holds for the Reynolds stresses. Both numerical domains reproduce the turbulent characteristics accurately. The LES overpredicts the axial stresses in the vicinity of the wall marginally. Since only small deviations occur, the 2.5D case is suitable for reactive studies and is considered for the remainder of this study.

4.2. Hotflow results

Fig. 7 displays the mean axial velocity profiles at different axial positions in the first row, while the Reynolds stresses are depicted in the last two rows. Beside averaging for 100 ms, the data is also circumferentially averaged. The axial velocity profiles are well captured in the reacting LES, including the effect of widening of the turbulent reacting jet. Compared to the non-reacting velocity profiles in Fig. 6, a larger widening of the turbulent jet is observed, which is due to the gas expansion in the cone-shaped flame. While the predictions for both Reynolds stresses are accurate close to the jet exit, they slightly deviate downstream. These regions are not crucial for the FB consideration and are likely to improve steadily with longer averaging times. Note that the non-reacting fields ($T_{\text{cold}} = 300$ ms) are averaged three times longer than the reacting fields ($T_{\text{hot}} = 100$ ms).

Overall, the turbulent characteristics in the reacting LES are in good agreement to the experiments.

5. Characteristics of the steady flame

After careful validation of the LES against two experimental setups with non-reacting and reacting measurements, we investigate the characteristics of the turbulent premixed hydrogen flame under lean conditions before the FB event. The aim here is to understand the steady flame properties and to link these to existing studies in the field of turbulent premixed hydrogen combustion. The copper tube (case A: $D = 20$ mm and $\Phi = 0.6$) is considered for this purpose since the FB simulations are based on the same setup.

Hydrogen-specific burning characteristics of a stable operating point are first described. The bulk velocity u_b is kept constant at $u_b = 10.2$ m/s. It is assured that the LES is at a statistically steady state by realizing two-flow through times over the entire domain before the data is acquired.

5.1. Salient characteristics of a turbulent premixed hydrogen flame

Essential aspects of hydrogen flame are derived from instantaneous contour plots of normalized heat release, mass fraction of H_2, temperature and mixture fraction contained in Fig. 8. The mixture fraction is defined as

$$Z = \frac{Y_{H_2} + \nu\left(Y_{O_2,air} - Y_{O_2}\right)}{1 + \nu Y_{O_2,air}}, \tag{7}$$

where Y_{H_2} and Y_{O_2} are the mass fractions of hydrogen and oxygen, respectively. The stoichiometric coefficient ν is fixed to eight referring to hydrogen combustion [38]. An equivalence ratio of $\Phi = 0.6$ equals a mixture fraction $Z = 0.017$ in the equilibrate state. It becomes obvious from Fig. 8(d) that the mixture fraction exceeds the equilibrium value, especially in convexly formed flame segments which are oriented

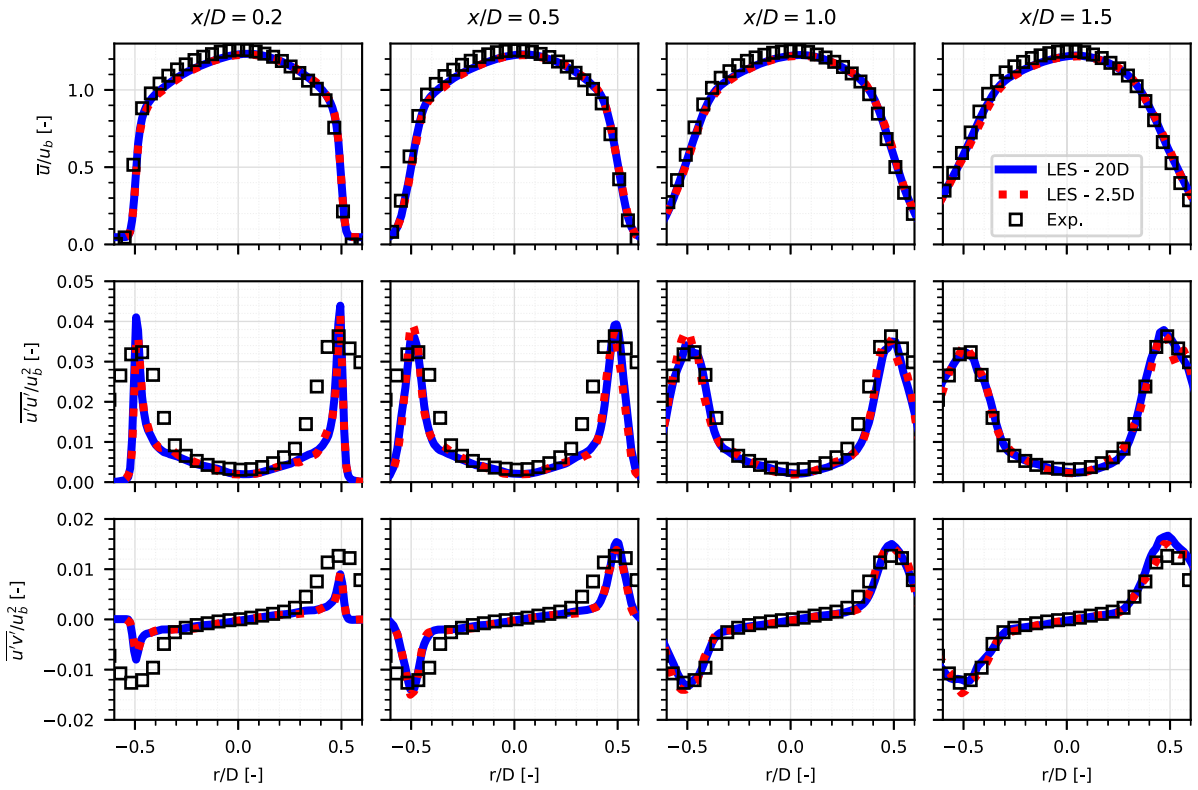

Fig. 6. Comparison between PIV measurements (squares) and two LES domains (long (blue) and short (red)) in predicting velocity profiles (first row) and Reynolds stresses (axial (second row) and shear stresses (third row)) downstream of the jet exit (column-wise). Note the change of the magnitude of one order in y-direction.

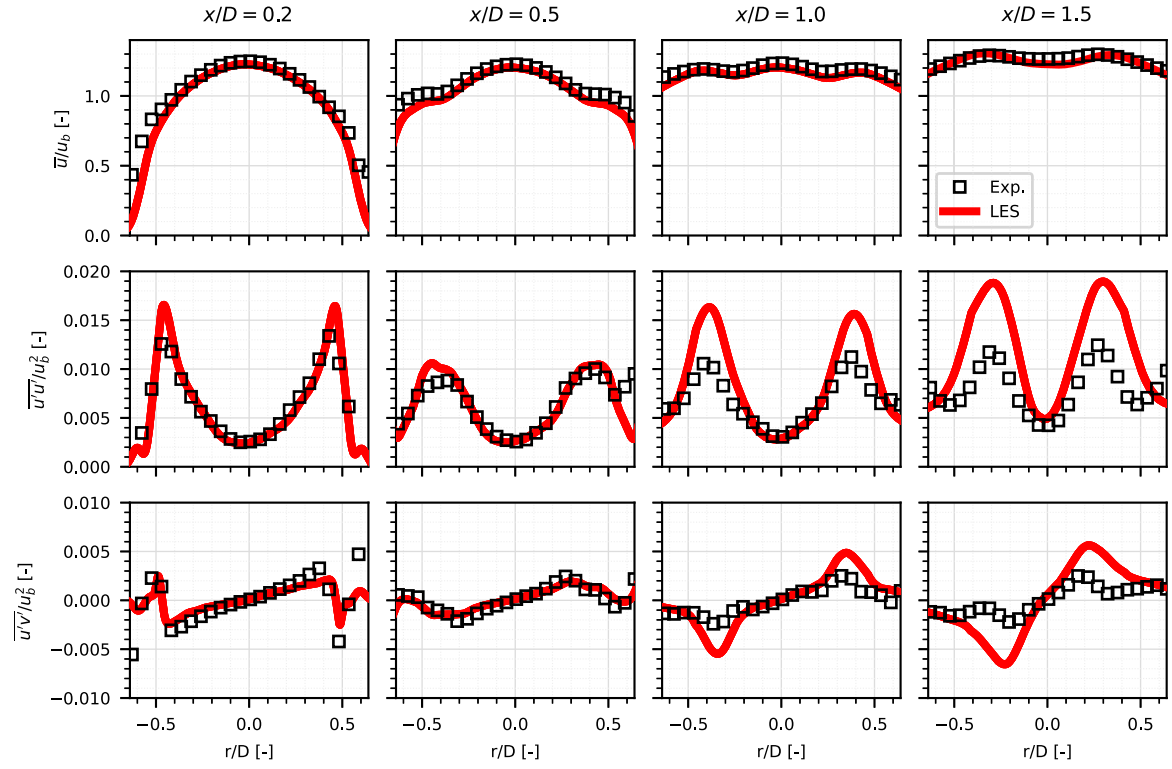

Fig. 7. Validation of reacting flow field at different streamwise positions along the flame height (columns). First row: axial velocity. Second row: axial Reynolds stresses. Third row: Reynolds shear stresses.

towards the unburnt mixture. This is in line with the observation of locally higher burning rates in positively curved flame segments, while lower burning rates up to local flame extinctions are found in opposite curved regions (Fig. 8(a)). As a direct consequence, super-adiabatic flame temperatures, which are colored pink in Fig. 8(c), are mainly found in convexly curved regions. These findings are in line

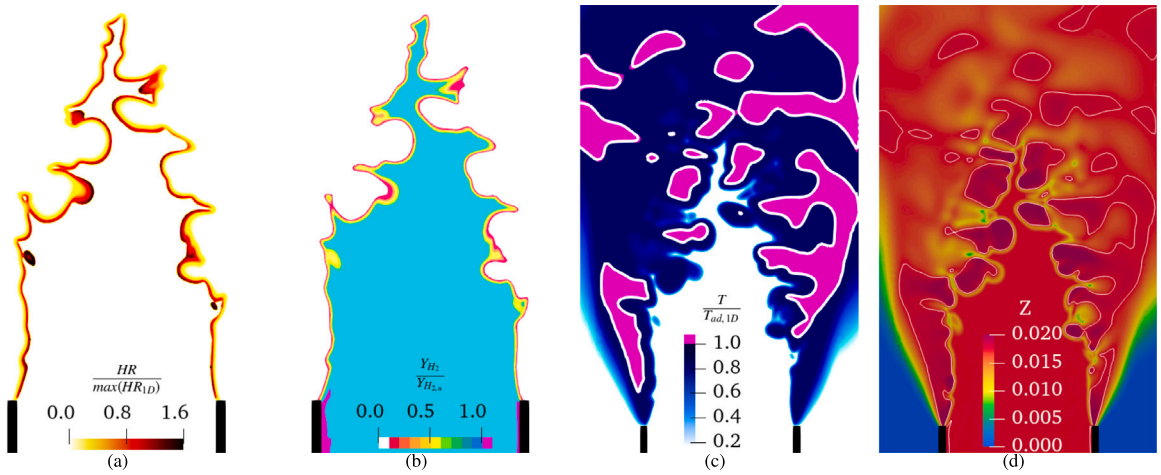

Fig. 8. Instantaneous contour plots at the same temporal instant of (a) HR normalized by the maximum value of a 1D, laminar, unstretched flame indicating distinct regions of super-adiabaticity, (b) mass fraction of H_2 normalized by its unburnt value featuring locally increased H_2 concentrations and (c) temperature normalized by the adiabatic flame temperature of a 1D flame with highlighted regions $T/T_{ad} > 1$ (super-adiabatic temperatures). Note that the thermal boundary layer in the tube is not displayed. A detailed view of the thermal boundary layer is found in Fig. 18. Larger and smaller mixture fraction values in relation to $Z = 0.017$ (fully mixed, white contourlines) are observed (d). Similar to (b), an increase in mixture fraction towards the tube walls due to the Soret effect is seen.

with previous DNS studies [33,34,39]. Moreover, it is a first indicator of TDIs being present in this flame configuration. Qualitatively, the flame features known physical effects, namely increased burning rate in convexly curved regions, which also have been observed in the experiment [24].

Based on the normalized mass fraction of H_2 in Fig. 8(b), the progress variable c is defined as

$$c = \frac{Y_{H_2} - Y_{H_{2,u}}}{Y_{H_{2,b}} - Y_{H_{2,u}}} = 1 - \frac{Y_{H_2}}{Y_{H_{2,u}}}, \tag{8}$$

where $Y_{H_{2,u}}$ and $Y_{H_{2,b}}$ is the mass fraction in the unburnt and burnt gas mixture, respectively. Since hydrogen is consumed by the flame as the mixture fraction value does not exceed the stoichiometric value of $Z = 0.028$, the mass fraction of hydrogen in the burnt gases reduces to zero, which leads to the last expression in Eq. (8). More hydrogen is clustered towards the wall expressed by the pink regions (norm. Y_{H_2} greater than unity) as shown in Fig. 8(b). Even with relatively low wall temperatures the Soret effect becomes significant and cannot be neglected. As will be described in more detail in Section 6, the Soret effect increases the equivalence ratio at the wall locally leading to higher flame speeds in FB-prone regions.

Based on 1D laminar flame calculations, the maximum heat release is found at $c = 0.7$. Unless otherwise stated, the isocontours of the flame refer to this value.

5.2. Turbulent flame speed

According to Attili et al. [40], a turbulent flame speed is derived based on the consumption speed, which is

$$s_c = -\frac{1}{A_0 \rho_u Y_{H_{2,u}}} \iiint_V \dot{\omega}_{H_2} dV, \tag{9}$$

where ρ_u and $Y_{H_{2,u}}$ refer to the unburnt density and mass fraction of H_2 in the mixture, respectively. The surface A_0 corresponds to the averaged flame surface assessing the mean progress variable at $c = 0.7$. To evaluate a turbulent flame speed along the streamwise direction, the flame is divided into discrete number of volumes. Within each volume both the volumetric integral of the net reaction rate of H_2 and the flame surface A_0 are computed. Besides, the stretch factor I_0 is determined, which accounts for the stretch affects (namely strain and curvature) on the flame surface:

$$I_0 = \frac{s_t}{s_l} \frac{A_O}{A_t} \tag{10}$$

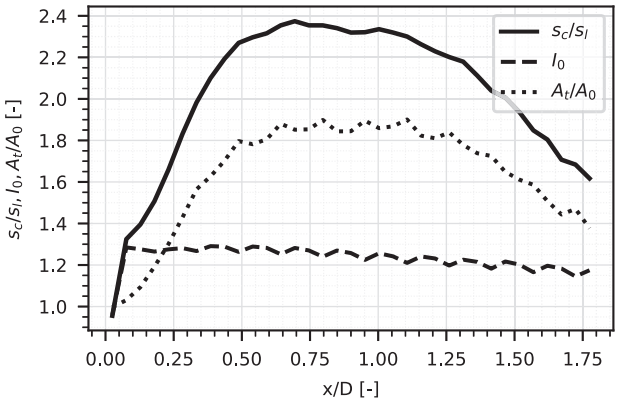

Fig. 9. Different ratios over the flame height: (i) turbulent flame speed to laminar flame speed (solid), (ii) instantaneous to averaged flame surface area (dotted), (iii) stretch factor I_0 combining (i) and (ii) (dashed).

Similar to A_0, the instantaneous turbulent flame surface A_t at a particular progress variable is determined in each volume.

The progression of the turbulent flame speed across the flame height is shown in Fig. 9: first, a steep increase up to 2.4 times the laminar flame speed within $x/D < 0.7$ and then it slowly decreases towards the flame tip. While qualitatively the same trend is seen for the area ratio between the instantaneous and averaged flame area, the stretch factor decreases linearly along the flame height. Thermo-diffusive stable flames, such as methane/air flames, possess stretch factors around unity. Hence, the increase in turbulent consumption speeds is solely due to the increase in flame surface area (A_T/A_0), which is driven by turbulence [40]. Hydrogen/air flames, however, which are subject to intrinsic flame instabilities, namely TDIs, feature stretch factors above unity. The increase in turbulent consumption speed is not only caused by turbulence, but also by intrinsic flame effects. This flame configuration exposes intrinsic flame instabilities, which are a main contributor to flame flashback as shown in Section 6.

5.3. Flame stretch

A flame moving in a turbulent flow field is generally subjected to flame stretch K which is defined as the sum of tangential strain rate

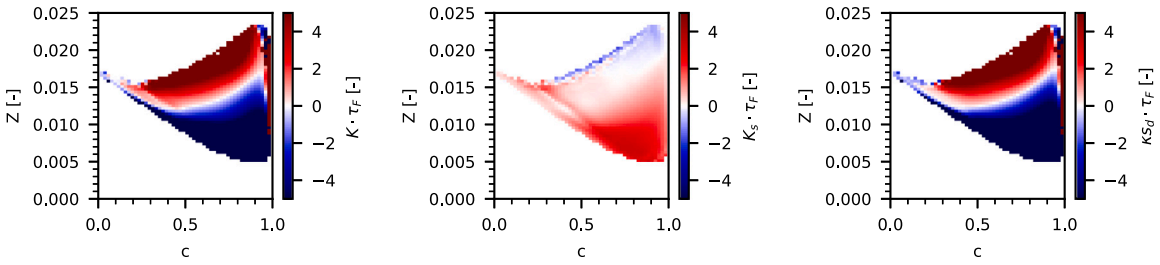

(a) Flame stretch (b) Strain term (c) Curvature term

Fig. 10. Mixture fraction Z and progress variable c weighted by flame stretch (a), strain term (b) and curvature term (c). The TUD flame is governed by curvature effects.

and the curvature term:

$$K = s_d \cdot \kappa + K_s, \tag{11}$$

where the former describes the tangential strain rate

$$K_s = \nabla \cdot \mathbf{u} - \mathbf{n} \cdot \nabla \mathbf{u} \cdot \mathbf{n}, \tag{12}$$

The latter defines the curvature term multiplied by the flame displacement speed and is given by

$$\kappa = \nabla \cdot \mathbf{n}. \tag{13}$$

Fig. 10 shows the effect of the tangential strain rate and the curvature on mixture fraction fluctuations. Mixture fraction and progress variable are weighted by the components of the flame stretch for this purpose. Starting with the curvature (Fig. 10(c)), positive curvature causes increased mixture fraction values, while lower mixture fractions are observed in negatively curved flame segments. For low values of the progress variable, the mixture fraction is close to its nominal value in the equilibrium state ($c < 0.2$). The distribution of the mixture fraction becomes wider as the flame evolves in the progress variable space. The exact opposite behavior is identified in the strain term where negative (positive) tangential strain rates relate to higher (lower) mixture fraction fluctuations (Fig. 10(b)): the flame surface area is generated due to curvature effects while negative strain rates destroy flame surface area locally. However, curvature dominates over strain effects as seen in Fig. 10(a). Positive flame stretch accounts for high mixture fraction fluctuations whereas negative flame stretch leads to low mixture fraction fluctuations.

In summary, the turbulent premixed hydrogen flame exhibits H_2-specific characteristics such as increased burning rates caused by TDIs. Although these features have already been described in several DNS studies [33,34,41], we scrutinize the H_2-specific effects as we identify them as crucial for the FB event in the following.

5.4. Turbulent flame characteristics and their relation to intrinsic flame instabilities

Synergistic interaction between TDIs and different turbulent intensities was studied experimentally [42]. Lapenna et al. showed that the stretch factor increases significantly with increasing intensity. To relate our numerical results to the findings of the experimental Bunsen burner study from Lapenna et al. we compute the ratio of the axial turbulent intensity at the burner axis to the laminar flame speed ($u'/s_l \approx 0.6$). Based on this ratio, a stretch factor around $I_0 = 1.3$ is found which is in very good agreement to the stretch factor obtained in Section 5.2, cross-validating our numerical results.

The flame-turbulence interaction is characterized by computing the turbulent Karlovitz number at the flame isosurface $c = 0.7$. The Karlovitz number is given by:

$$\mathrm{Ka} = \left(\frac{l_f}{\eta}\right)^2, \tag{14}$$

where l_f is the laminar flame thickness and the Kolmogorov length scale η is estimated by:

$$\eta = \left(\frac{\tilde{\nu}^3}{\tilde{\epsilon}}\right)^{\frac{1}{4}}. \tag{15}$$

The turbulent dissipation rate ϵ writes:

$$\tilde{\epsilon} = \tilde{\nu}\left(\overline{\frac{\partial \tilde{u}_i'}{\partial x_j}} + \overline{\frac{\partial \tilde{u}_j'}{\partial x_i}}\right)^2. \tag{16}$$

The Karlovitz number is $Ka \approx 5$, meaning that this flame would fall into the regime of the thin reaction zone: small turbulent eddies are capable of entering the flame front and altering the inner structure. Moreover, the turbulent flow is characterized by the largest scales, namely the integral length scale, which are computed from a two-point correlation ($l_f = 4.71$ mm). The smallest turbulent eddies (Kolmogorov length scales) are based on Eq. (15) ($\eta = 0.21$ mm). Both length scales are related to thermo-diffusive instabilities by expressing a turbulent wavenumber ($k = \frac{2 \cdot \pi}{l_{turb}}$). With that, we can estimate the growth rates based on a linear dispersion relation from 2D laminar flames studied by Berger et al. [41]. The integral length scales amplifies the growth of the TDIs, while the wavelength of the Kolmogorov length scale predict a damping behavior. However, the most amplified turbulent length scale is found at around $l_{turb} = 1.88$ mm. In general, the flame is subjected to different turbulent length scales, which in turn trigger intrinsic flame instabilities as analyzed in Section 5. The influence of these structures on flashback is investigated in the following.

6. Analysis of flame flashback

In the previous section, we scrutinized TDI-effects in the steady state condition, which are the main driver for FB as will be shown in the following. Now we examine how these effects behave during the transient flashback process. This section covers phases ii–iv of Fig. 1. Firstly, we describe global characteristics of the flame during flashback. Secondly, local characteristics, namely the flame leading finger, which contains the flame leading points, are analyzed. This is followed by the flame-flow interactions during the flashback process.

6.1. Global upstream flame propagation during flashback

As for the experimental procedure, the velocity is also reduced in the LES at the velocity inlet from $u_b = 10.2$ m/s to 6.0 m/s within $t = 30$ ms (Fig. 11). In the experiments, it takes several minutes, starting from a stable operation point until the velocity is reduced to an extent that the flame propagates upstream. This is infeasible to reproduce in the LES due to computational costs. This is due to the fact that the experiments remain at one operating point significantly longer than in the LES (in the order of minutes). This is the main difference in the ramp behavior between the experiments and the LES, where in the latter the Reynolds number is continuously decreased, while in the experiments, it is a sequence of step functions.

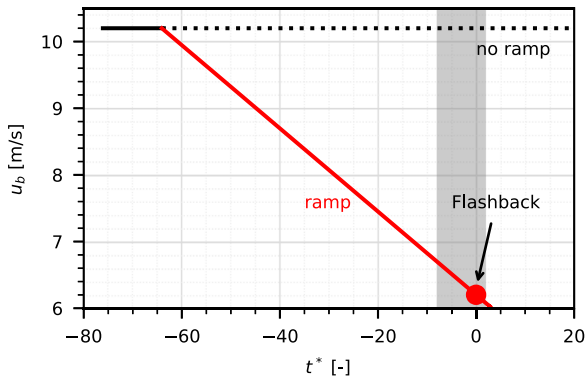

Fig. 11. Velocity ramp to trigger the FB event: 20 ms (red). The red marker indicates the flashback event. Gray colored area covers the transition from unconfined to confined FB (Fig. 12). The dotted line represents the steady state simulation.

We select a ramp with a moderate gradient ($du/dt = -15\,\mathrm{m/s^2}$ in Fig. 11) based on preliminary studies (Fig. D.27 in the appendix). A steeper gradient leads to ramp-induced flow separations at the wall, while the flashback behavior is unaffected by a smoother gradient. However, we notice that the global and local trends of FB are similar and thus independent of the ramp gradient, except for the time when flashback occurs. The dot represents the time when flashback occurs in the LES (Fig. 11). As soon as the axial coordinate of the flame iso-surface at $c = 0.7$ falls below zero, i.e. in the mixing tube, we refer to flashback with the related time t_{FB}. Flashback is obtained for a bulk velocity of $u_b = 6.2\,\mathrm{m\,s^{-1}}$, which is below the experimental value ($u_b = 9.0\,\mathrm{m\,s^{-1}}$). As pointed out in Sections 2 and 3, a number of uncertainties in numerical modeling (duration of the velocity ramp, flame resolution, wall temperature) and the experimental procedure (stochastic scatter, position of the thermocouple, mass flow controller settings) are present. The impact of the wall temperature is clarified in Section 7.2. Note that the time is normalized by

$$t^* = \left(t - t_{FB}\right)/\tau_f, \tag{17}$$

where t_{FB} corresponds to the time when FB occurs and τ_f is the flame time ($\tau_f = \delta_f / s_l$). If t^* is smaller than zero, flame flashback has not yet taken place, whereas values greater than zero refer to FB.

Apart from the ramp, the dotted black line indicates the stable simulation where the bulk velocity ($u_b = 10.2\,\mathrm{m/s}$) is unaltered (no ramp is applied). We performed this LES to check if FB occurs within the same physical time featuring the same temporal inflow conditions. Here, the flame remains outside the mixing tube. Fig. 12 shows the global upstream flame propagation from being unconfined in the first image to an confined state in the last frame. Note that only the transition time of Fig. 11 is shown (gray area). Next to each image, the leading flame finger is plotted, which is analyzed in more detail in Section 6.3.1. In general, the hydrogen flame undergoes intrinsic instabilities such as Darrieus–Landau and thermo-diffusive instabilities (TDI), which are detailed for this flame in Section 5 [33,43]. The heterogeneous distribution of the heat release over the flame surface is a strong indicator for TDIs (Fig. 12). Similar to Section 5 and Fig. 8, high values of the heat release (red) are observed, where the flame is convexly shaped towards the unburnt mixture, while lower values are seen in concave (green, yellow) cusp regions. In the lower part of the flame (directly downstream of the jet exit), elongated flame fingers with enhanced heat release occur, whereas no clearly definable structures of the TDIs in the upper parts of the flame surface are identified.

During the ramp, the flame height decreases. Moreover, we observe that longitudinally oriented flame fingers along the burner rim are formed by low velocity streaks leading to a significant increase in heat release ($t^* = -6.73$). The flame-flow interaction with the identification of a low velocity streak is analyzed in Section 6.3.4. Starting at $t^* = -5.53$, the newly formed flame leading finger interacts with the approaching flow up to the point where it jumps into the mixing tube and propagates further upstream. From here, the well-understood confined BLF process starts with its characteristics such as boundary layer separation and generation of a recirculation zone ahead of the flame (green isosurface in Fig. 12h–i) which is responsible for the adverse pressure gradient [3,44–47].

6.2. Description of turbulent structures and the identification of the ejection event

Turbulent wall-bounded flows are characterized by quasi-coherent structures, which occur at different spatial and temporal instances along the boundary layer in the mixing tube. Among these are low speed streaks, sweep events and the counterpart ejection events. As these turbulent structures might affect the FB behavior, this section aims to identify them.

Based on the energy equation of turbulent motion, turbulent production is defined as [48]:

$$P = -\overline{u_i' u_j'}\frac{\partial \overline{u_i}}{x_j}. \tag{18}$$

Since the round jet is axisymmetric, we transform the Cartesian coordinates into Polar coordinates. For the identification of a low velocity streak, the radial and axial velocity components are considered. Wallace et al. and Willmarth et al. derived a method, called quadrant analysis, which assign the product of the Reynolds stresses ($u_r' u_x'$) to a quadrant dependent on the sign of the velocity fluctuations [49,50]. The ejection event, which transports slow flowing fluid away from the wall, is identified by the negative axial velocity fluctuation, while the radial component is positive. This is assigned to the second quadrant where $u_x' < 0$ and $u_r' > 0$. Consequently, the product is negative, leading to the production of turbulent kinetic energy.

In order to identify the ejection event during FB, a characteristic probe point is selected at the jet exit ($x = 0\,\mathrm{mm}$) with a radial distance of 0.5 mm away from the wall and at a fixed circumferential position. Fig. 13 shows both the axial and radial velocity components recorded at this probe point. Prior to flashback, an ejection event takes place (green filled area). The temporal sequence is illustrated: first, the low velocity streak is approaching the flame before the flame is capable of entering the mixing tube. Due to the ejection event, slow flowing, preheated and H_2-enriched fluid from the wall is transported to regions where the flame can exist (clearly outside the quenching distance). This leads to a higher reactivity of the flame with a more bended flame front. At the same time, the ejection event increases the vorticity as it acts as a source term for turbulent kinetic energy as will be discussed in Section 6.3.4. It is this event that enables the flame upstream propagation into the mixing tube. The next section investigates these effects in more detail via the flame leading point to confirm this hypothesis.

6.3. Local analysis of the flame leading finger

The local flame leading finger is already introduced in Fig. 12. The characteristics of this flame finger are first investigated by capturing the position of the flame leading point (FLP) and then examining the interactions between the flame and the flow during FB.

6.3.1. Definition of the flame leading point

The transient behavior from unconfined to confined flashback is described by monitoring the FLP shown in Fig. 14. The FLP is defined as the maximal net reaction rate of hydrogen (i: $\max(\dot{\omega}_{H_2})$) on the flame iso-surface (ii: $c = 0.7$) evaluated within the predetermined geometric constraints (iii: $3.5 < \Theta < 4.1$, iv: $x < 4\,\mathrm{mm}$, v: $r < 11\,\mathrm{mm}$) corresponding to the FLF. The FLP is computed with regard to the cylindrical coordinate system at the center location of the tube

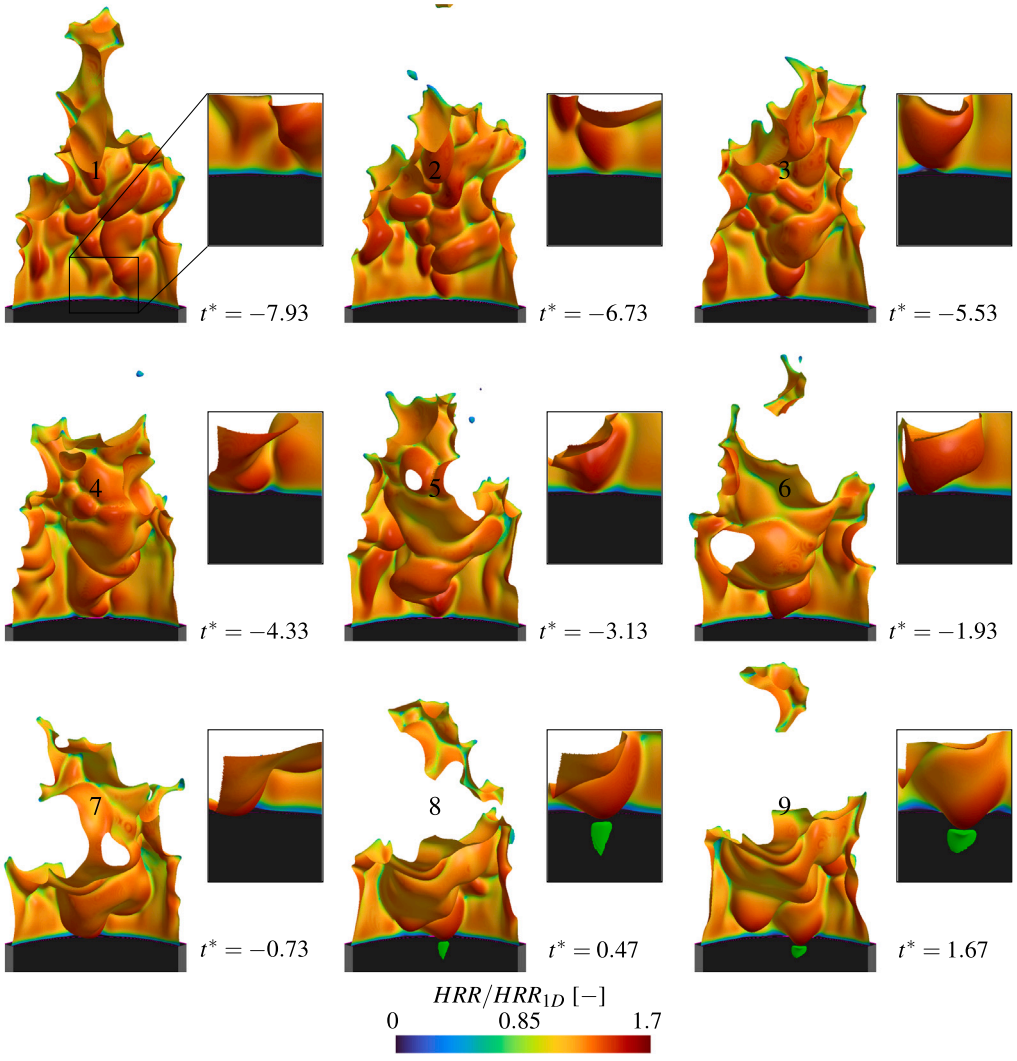

Fig. 12. Flame upstream propagation during FB, showing a 90°flame segment. Each snapshot evolves with $\Delta t = 0.5$ ms. Normalized HR is analyzed on the iso-contour at $c = 0.7$. Flame flashback occurs between $t^* = -0.73$ and $t^* = 0.47$, while the onset of flashback even starts earlier. Once the flame enters the mixing tube, it continues to propagate further upstream and a recirculation zone is formed (green isosurface) due to the adverse pressure gradient.

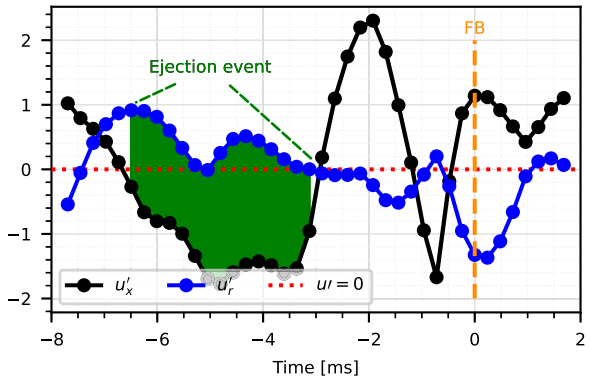

Fig. 13. Identification of the ejection event. Turbulent fluctuations in axial (u_x') and radial (u_r') directions are recorded at one characteristic point. Ejection event is characterized by positive radial fluctuations and negative axial fluctuations (green area). The ejection event occurs prior to FB.

exit, pointing in the axial downstream direction (Fig. 2). The FLP is characterized by the three coordinates (axial, radial and circumferential position in Fig. 14).

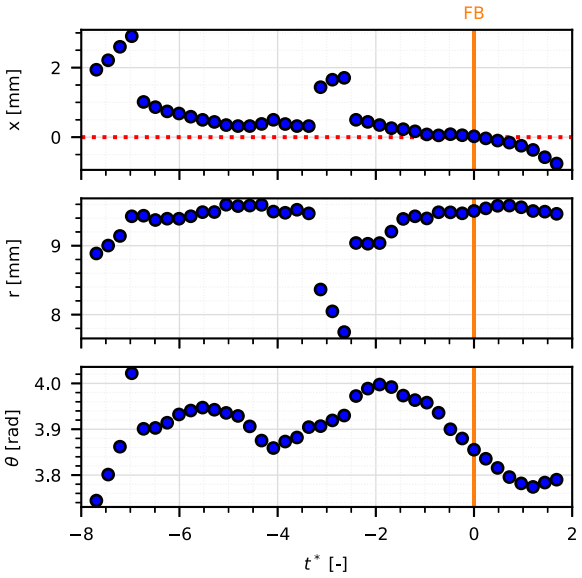

Fig. 14. Description of FLP position by monitoring its three coordinates at which the maximum reaction rate of hydrogen occurs. Orange marker displays FB in the LES.

Initially, both the axial and radial position increase, while the FLP is moving along the burner rim. This is highlighted by the Θ location, where no fixed location of the FLP could be identified. During the same time ($t^* < -7$), the FLP is located at a distance of at least 2.0 mm from the inner edge of the tube (Fig. 14). This behavior indicates a stable regime, up to $t^* = -6.73$ where the radial position becomes constant and the axial distance decreases towards the mixing tube. This is also the starting point of the transition from unconfined to confined BLF. Around $t^* = -3$, the position of the FLP rapidly changes to a more inward bended flame ($r = 8$ mm) with an slightly raised FLP ($x = 1.8$ mm). The actual FB occurs once the axial position is below the red dashed horizontal line at $t^* = 0$ (orange marker). Once the FLP is in the tube, it moves approximately 0.48 mm off the wall further into the pipe, changing its circumferential position slightly over time.

In the following, the transition from unconfined to confined FB is studied locally for the flame finger.

6.3.2. Transition of the flashback process

The transition process is divided into two major parts. First, the flame propagates into the flame normal direction towards the jet center, while, secondly, the flame enters the mixing tube in the boundary layer after it was perpendicular to the flow direction. Fig. 15 describes the transition of boundary layer flashback from unconfined to a confined state. The isolines are extracted at $c = 0.7$ on the 2D plane that intersects the FLP as defined in Section 6.3.1. The first timestep is colored in green showing a non-curved flame, whereas the transition is shown in red. Note that an increase in opacity is equal to the progressive time. With increasing time, the flame first propagates towards the center of the mixing tube, while it is more bended towards the fresh gases, before the flame enters the mixing tube. At one instant during the transition, the flame is quasi perpendicular to the axial flow velocity which eventually facilitates the upstream propagation close the wall. Next, a curved flame segment is formed in the vicinity of the wall, which propagates upstream into the mixing tube with increased consumption speed s_c. From here on, the radial position of the FLP hardly changes. The flame enters the mixing tube at a distance $\delta_q = 0.48$ mm which is in the order of the head-on quenching distance ($\delta_q = 0.22$ mm) obtained from a 1D laminar flame HOQ computations (not shown). Moreover, the flame enters the mixing tube at the position where the flame stretch rate becomes high. Previous studies on HOQ indicate that the quenching distance is approximately two times smaller compared to the side-wall quenching [51]. This explains why the flame does not move closer to the wall when propagating in the tube. The blue isoline clearly shows the flame in the tube with the properties known from the confined state [3,44–47]. Next, we analyze the temporal behavior of substantial quantities in the FLP during BLF.

6.3.3. Flame leading point behavior during the transition

Various physical quantities are evaluated in the FLP and grouped by (i) HR, reaction rate of H_2 and mixture fraction, (ii) flame stretch and (iii) the comparison between flame and flow speeds in Figs. 16(a)–16(c), respectively. As already mentioned in Section 6.3.1, the FLP is defined on the flame iso-surface $c = 0.7$ based on the maximum reaction rate of hydrogen in 1D adiabatic flames. However, the maximum in the bunsen burner configuration is shifted towards the burnt region ($c = 0.8$), while the maximum of the heat release rate is found at $c = 0.5$ due to the dilatation. Since only the absolute values of the HR and the reaction rate are affected by the selection of the iso-surface, but not the curve progression, we keep the value of $c = 0.7$.

Similar trends are identified between the HR, net reaction rate and mixture fraction in Fig. 16(a). Each quantity significantly exceeds the nominal values of an 1D adiabatic flame ($HR/HR_{1D} > 1$, $\dot{\omega}_{H_2}/\dot{\omega}_{H_2,1D} > 1$ or the unburnt mixture fraction ($Z/Z_{eq} > 1$), indicating that TDIs are active in the FLP. The peak in the mixture fraction occurs before the peaks in both HR and reaction rate are observed. An increase in mixture fraction due to both the low Lewis number effect and the Soret effect leads to higher burning rates, which in turn accelerates the flame propagation. Shortly before the flashback, all values increase significantly ($-1 < t^* < 0$), which eventually leads to the flashback. This rise in all quantities is triggered by the ejection event (Section 6.2).

The highest reaction rate of hydrogen is always observed in positively curved flame segments (Fig. 16(b)), whereas the strain term is below zero, counteracting against the curvature, and thus reducing the stretch rate in the FLP. Nonetheless, the curvature term outbalances the strain effects which results in solely positive stretch values in the FLP as already shown in the steady flame analysis in Section 5.3. During the flashback process, the flame is stronger curved, which is equivalent to an increase in flame surface area and thus, also in the turbulent consumption speed.

In order to relate the flame velocities to the flow velocities in the FLP during the transition, the flame displacement speed is plotted in Fig. 16(c). The flame displacement speed s_d describes the flame movement relative to the flow in the flame normal direction and is derived from the transport equation of the progress variable c(Appendix E):

$$s_d = \frac{1}{\rho\,|\nabla c|}\left[\bar{\dot{\omega}}_c - \frac{\partial}{\partial x_i}\left(-\bar{\rho}\left(\left(\bar{D}_c + \frac{\mu_t}{Sc_t}\right)\frac{\partial \tilde{c}}{\partial x_i} - \frac{1}{Y_{H_{2,u}}}\frac{\bar{D}_{c,t}}{\bar{\rho}\tilde{T}}\frac{\partial \tilde{T}}{\partial x_i} + (1-c)\,\tilde{V}_c\right)\right)\right], \tag{19}$$

where the reaction rate, both the mass and thermal diffusion and the correction velocity are considered. To account for the thermal expansion along the flame front, the flame displacement speed is weighted by density ratio: $sd^* = s_d \cdot \rho/\rho_u$ with ρ_u being the density of the reactants. The flame displacement speed slightly increases over time in the transitional area, which however reaches a local maximum shortly before FB occurs. We derive a flame speed based on the relation of the flame displacement speed ($s_d = s_f - \mathbf{u}\cdot\mathbf{n}$) in Fig. 16(c), which is identical to the work of Chen et al. [10]. The normal vector $\mathbf{n}$ of the flame points into the unburnt mixture. The velocity is therefore negative. If the flame speed is positive ($s_f > 0$), the flame moves upstream, while a downstream flame propagation is achieved when the flashback speed is negative ($s_f < 0$). Over the entire flashback process, the flame speed s_f is positive, which implies an upstream flame propagation during the transition. The curve of the flame speed follows the characteristics of the axial coordinate of the FLP (Fig. 14), which increases towards the end of time due to the confinement of the flame in the mixing tube.

In summary, the transition process starts with the formation of the flame leading finger which leads to a flame upstream propagation, meaning that the FLP in the flame finger propagates upstream to the jet exit (Fig. 14). Both curvature and heat release simultaneously increase in the flame finger, which results in higher flame speeds. This flame-flow interaction is discussed in detail in the next section.

6.3.4. Flame-flow interactions

We analyze the flame-flow interactions during FB and first show four time frames of the velocity field at a cylindrical plane ($r = 9.5$ mm) together with the flame front at $c = 0.7$, which is colored by the heat release rate (Fig. 17). In the first image ($t^* = -6.73$), both the newly formed flame finger and the approaching low velocity streak upstream of the flame leading finger are clearly visible. The red region of the flame surface indicate high burning rates. Within the next frames, the low velocity streak encounters the flame front, resulting in a flame upstream propagation. The flame leading point moves along the low velocity streak. According to Fig. 17, we state that the low velocity streak triggers the flashback event and is mainly responsible for the flame upstream propagation. Similar trends have also been observed in the experiments [24].

The image matrix (Fig. 18) contains the flow velocity (1st column), the normalized mass fraction of hydrogen (2nd column), the temperature (3rd column) and the vorticity magnitude (4th column)

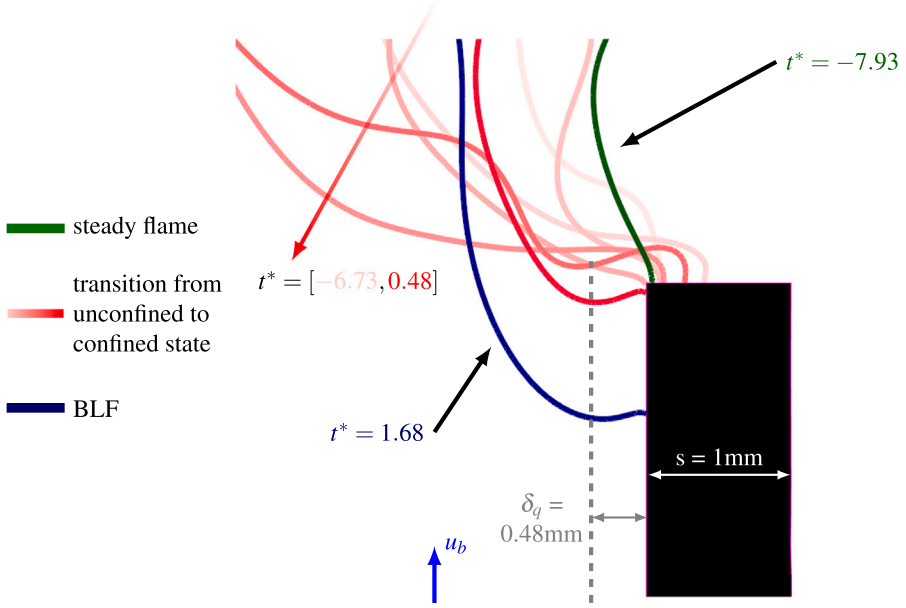

Fig. 15. Isolines at $c = 0.7$ during the transition of BLF: starting from stable conditions (green) over the transition process (red) to a confined state (blue). The flame enters the mixing tube at the quenching distance ($\delta_q = 0.48$ mm).

at distinctive timestamps (rows). The 2D planes intersect with the FLP, meaning that they are dynamically adjusted. In the first time steps ($t^* = -7.93$), a stable flame shortly prior to FB is observed with imperceptible features in all four quantities (u_x, Y_{H_2}, T, ω_{vort}). Afterwards, a significant change is observed ($t^* = -6.73$): the velocity is reduced in the vicinity of the wall, while in the same area the mass fraction of hydrogen and the preheat temperature is increased.

A low velocity streak (ii) approaches the jet exit ($-6.73 < t^* < -0.73$: dark gray structures close to the wall). The low velocity triggers the flame to propagate towards the tube exit, resulting in a more curved flame segment. Not only the reduction in the velocity is responsible for the curved flame, but also the simultaneous rise in the preheat temperature of the fresh gases in the mixture and mass fraction of hydrogen. All three quantities ($u_x \downarrow$, $T_p \uparrow$, $Y_{H_2} \uparrow$) lead to a more reactive flame. We refer to this as a low velocity streak caused by an ejection event. It ejects slow flowing fluid from the wall outwards. Directly at the wall, most of the hydrogen is accumulated due to the Soret effect, where also the highest temperatures are found due to the heating process of the wall by the flame. This slow flowing, high-temperature fluid with an increased content of hydrogen is transported to regions where the flame can exist, clearly outside the quenching distance. An ejection event produces turbulence as it acts as a source term for turbulent kinetic energy which is why an increased magnitude of vorticity is seen (Fig. 18, 4th column, $t^* = -4.33$) [48]. The identification of the ejection event is found in Section 6.2. As a consequence of the ejection event, the flame responds with increased H_2-specific characteristics, such as increased curvatures, reaction rates, etc. (Fig. 16(b)). This behavior mainly corresponds to the phase iii (Fig. 1). It then leads to flame segments, which are perpendicular to the axial flow velocity (Fig. 18 at $t^* = -1.93$). Due to this orientation, the flame moves further towards the mixing tube and finally enters it along the turbulent boundary layer.

Simultaneously, a strongly increased adverse pressure gradient, induced by the flame, approximately 3 mm away from the wall is observed (Fig. 19, $t^* = -2.41$). Triggered by the low velocity and high vorticity values within the ejection event, the leading flame finger grows significantly. The growing flame leading finger induces an adverse pressure gradient in the transition area (Fig. 19, $-4.33 < t^* < -2.41$), which in turn decelerates the flow more strongly. Thus, the adverse pressure gradient facilitates flame upstream propagation in the flame normal direction and contributes decisively to flashback. We can therefore confirm the general assumption of the experimental work which observes a similar behavior of the flame-flow interaction in positively curved flame segments: a larger adverse pressure gradient is found at higher positive curvatures of the flame bulge [24]. The strong growth of the flame leading finger causes high curvatures of the flame in the region of the turbulent boundary layer ($t^* = -1.93$), which increases the local flame speed there, making it more prone to FB. Along the flame entering position, curvature values peak and thus cause the flame to propagate into the tube ($t^* = -0.97$). Finally, a small recirculation zone (Fig. 18: first column, iv, pink isoline) is formed at $t^* = 0.47$, growing over time, which is typically found for confined BL flashback process.

In summary, the transition process is initiated at around 2 mm upstream of the burner rim, while the flame moves at a wall distance of 0.48 mm into the mixing tube (order of SWQ). During this transition, the flame is significantly curved towards the unburnt mixture while the heat release rate increases. This mechanism is known for low Le number flows, such as hydrogen: intrinsic instabilities such as TDIs and DL enhance the burning rate when the flame convexly formed towards the fresh gases. This results in locally higher flame speeds, which in turn have a stronger influence on the approaching flow field and finally provoke FB.

7. Parametric variation of key parameters on flashback

We vary two parameters to study the impact on the FB behavior, while keeping all other settings unchanged. First, we set the Lewis number to unity so that all species diffuse with the same velocity. By this, we suppress the TDIs and exclude their impact on the flame, while performing the same velocity ramp with the identical turbulent flow. Second, we increase the wall temperature to a peak value of $T_W = 500$ K at the burner rim.

7.1. Unity Lewis versus non-unity Lewis number

Prior to the occurrence of flame flashback, the molecular diffusivity model is changed to the unity Lewis approach which implies that all species diffuse with the same velocity. The Lewis number is set to unity while a constant Schmidt number of 0.7 is utilized based on a Prandtl number in the burnt gases ($S_c = PrLe$ with $Pr = \mu c_p/\lambda$).

The turbulent inflow conditions are unaltered compared to the reference case. This means that in both cases the flame front is exposed

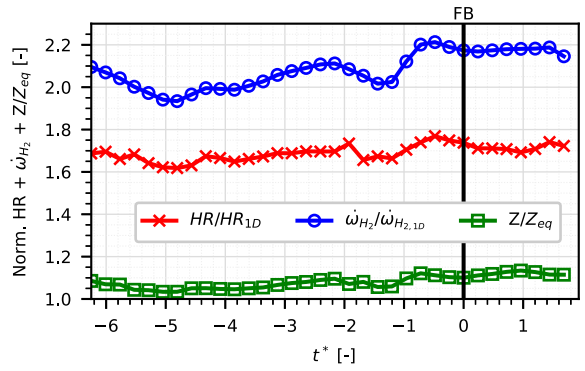

(a) Heat release rate, net reaction rate of H_2 and mixture fraction

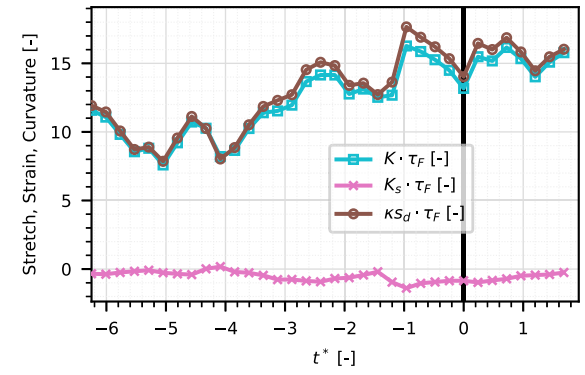

(b) Flame stretch

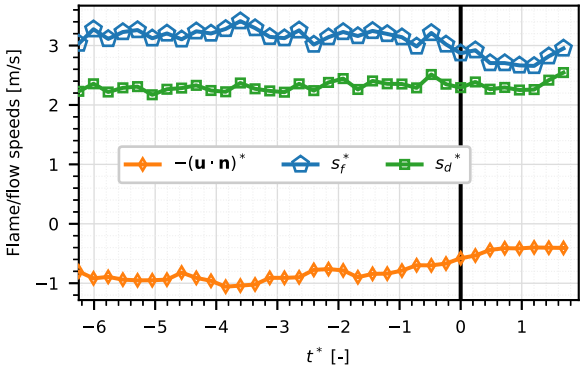

(c) Flame and flow speeds

Fig. 16. Temporal evolution in the FLP at $c = 0.7$. The black solid line indicates FB at $c = 0.7$.

to the same turbulent characteristics. Fig. 20 shows the isolines at the progress variable $c = 0.7$ at the same time step for $Le \neq 1$ (blue) and $Le = 1$ (red). While the flame enters the mixing tube and is positively curved for the non-unity Lewis number approach, the flame for the unity Lewis number is distinctively away from the jet exit. Moreover, the flame segment does not contain positive curved flame segments and the HR distribution along the flame is more uniform (not shown). In terms of magnitude of the HR, case 1 ($Le \neq 1$) has higher values than case 2 ($Le = 1$). We can clearly state that the flashback mechanism is driven by thermo-diffusive instabilities. Next to the sketch in Fig. 20, the PDF of the curvature term (a) and strain rate term (b) in the FLF is shown. The geometrical constraints of the FLF are already defined in Section 6.3.1. While the PDF of strain terms for both modeling approaches are relatively similar, the PDF of the curvature term differs

Table 3
Flashback occurrence as a function of (i) ramp steepness and (ii) thermal boundary conditions. The values correspond to the bulk velocity measured at the jet exit plane.

	T_w = 350 K	T_w = 500 K	T_w = adiabatic
u_b	6.2 ms^{-1}	9.1 ms^{-1}	10.2 ms^{-1}

significantly. This means the strain term is not affected by the non-unity Lewis number approach. However, the PDF of the curvature for non-unity Lewis is broader than for the unity Lewis number approach and higher positive values of curvature are observed. Due to the higher positive curvature values and, thus, the higher reaction rates, the flame enters the mixing tube, while the flame with unity Lewis remains above the burner exit.

Finally, we clarify whether the occurrence of the low velocity streak is irrespective of the Lewis number approach. Therefore, we choose a time instant closely linked to flashback for both diffusion models, where the vorticity is shown (Fig. 21). The main difference is that the two models respond differently to the flame/flow interaction (stretch and thus, the occurrence of the low velocity streak). While in the non-unity Lewis approach, a flame finger is formed which moves upstream towards the jet exit (Fig. 21(a)), the flame in the unity Lewis model is pushed away by the low velocity streak (Fig. 21(b)). Thus, these low velocity streaks always occur regardless of the Lewis number approach and are related to wall bounded flows both in reacting and non-reacting simulations. In summary, we confirmed that the flashback mechanism is mainly driven by TDI-effects.

7.2. Impact of thermal boundary conditions on flashback behavior: T_w = 350 K versus T_w = 500 K

We vary the wall temperature profile by maintaining the temperature distribution on the solid wall and only adjust the magnitude of temperature so that a temperature of 500 K is realized at the burner rim. All other settings, both numerical and physical, remain unchanged. The case $T_w = 500$ K undergoes the same velocity ramp and turbulent flow statistics as the reference case at $T_w = 350$ K, meaning that the turbulent inflow characteristics are identical. However, due to the increase in wall temperature, the viscosity increases, while simultaneously the density drops. Both attribute to a change in turbulent characteristics. According to Table 3, FB occurs at a bulk velocity of $u_b = 9.1$ m/s with preheated walls ($T_w = 500$ K). This corresponds to a difference of $\Delta u_b = 3$ m/s compared to the colder walls. The differences between the two simulations are briefly described below.

Both transition processes are shown in Fig. 22. While there is a time interval of $\Delta t = 0.5$ ms between the plots for the hotter wall case, the colder wall case is separated by $\Delta t = 1.0$ ms, meaning that the former FB transition time is significantly faster. However, the transition characteristics between both wall temperatures is similar. In the first time step, no clear flame finger is observed (less curvature), which is formed afterwards. The flame of the cold case enters the mixing tube further away from the wall. This behavior coincides with the quenching distances: it decreases as the wall temperature increases. Based on 1D flame computations, the head-on quenching distance for the hot case is approximately $\delta_q = 0.18$ mm, whereas a rising value is observed for the cold case ($\delta_q = 0.22$ mm). The radial distance of the FLP in the cold confined state is 0.48 mm, while the FLP of the hot case enters the mixing tube at 0.38 mm showing good agreement between the 3D turbulent and 1D laminar simulations. The reduced quenching distance facilitates the flashback significantly.

Fig. 23 shows the normalized temperature $\left(\left(T - T_w\right) / \left(T_\infty - T_w\right)\right)$, velocity and equivalence ratio at the jet exit line, intersecting the FLP and being normal to the wall as shown in Fig. 22. Again, the transition for the hot case is significantly faster in terms of flame propagation than the cold case since the flame is partially inside the mixing tube in the second frame (Fig. 23b). Flame entering is seen either by the

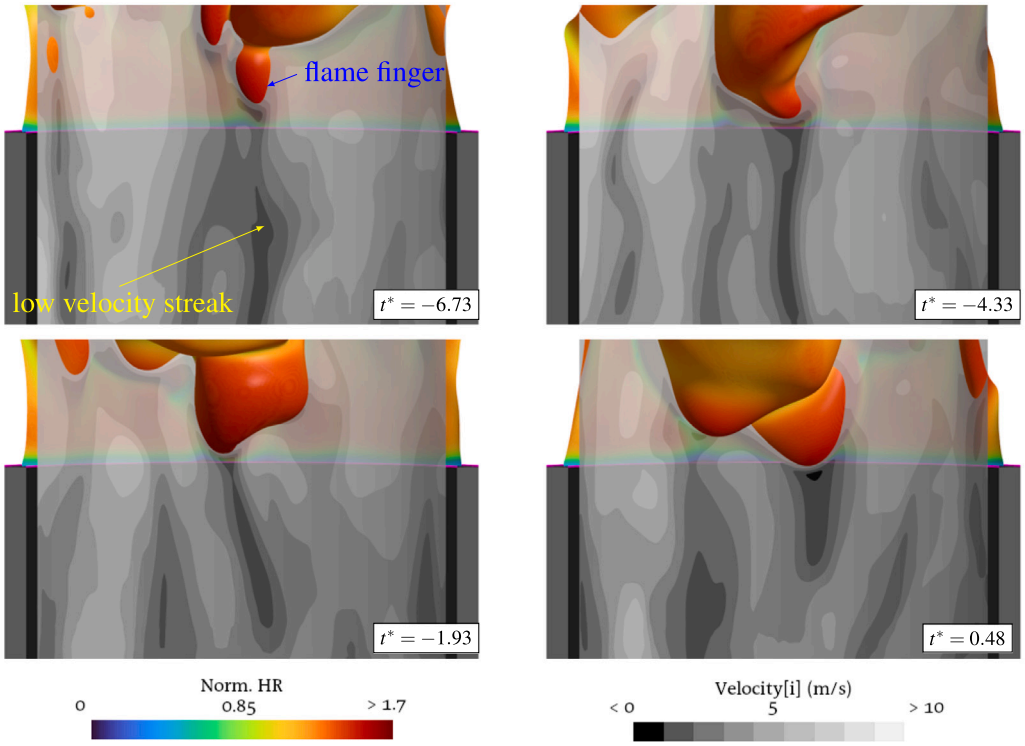

Fig. 17. Instantaneous velocity field on a cylindrical plane together with the flame front at $c = 0.7$.

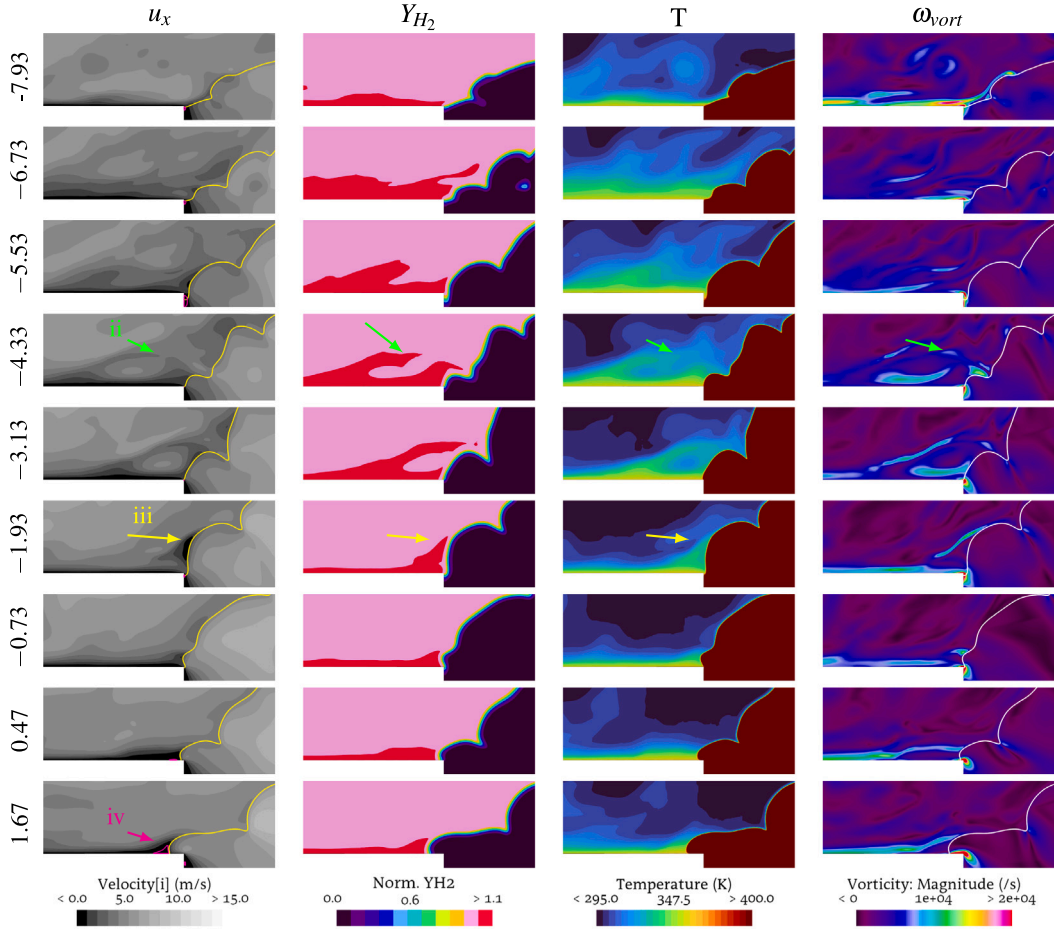

Fig. 18. Contour plots of velocity, mass fraction of hydrogen, temperature and vorticity are shown in the first, second, third and fourth column, respectively. The dimensionless time is displayed in each row.

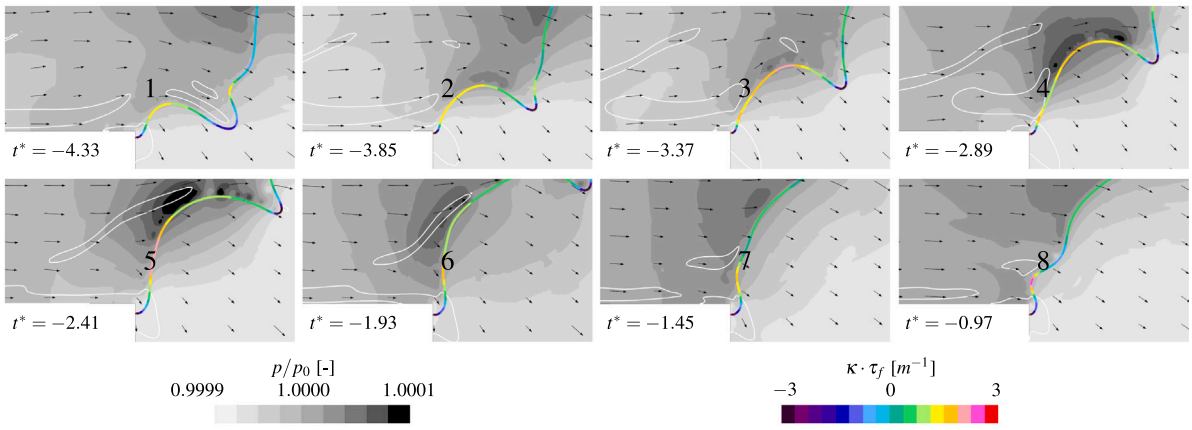

Fig. 19. Flashback process is shown by the pressure field and the flame isoline at $c = 0.7$, which is colored by curvature values. In addition, the vorticity isoline at $\omega_{vort} = 7000\,s^{-1}$ is displayed. A high adverse pressure gradient ahead of the flame at $t^* = -2.41$ is observed.

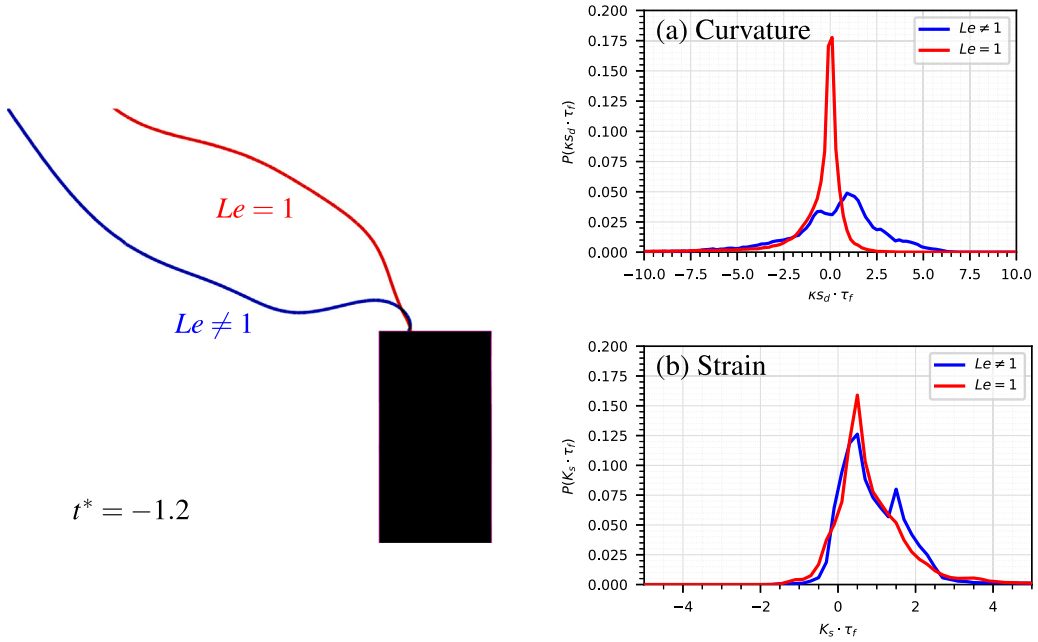

Fig. 20. Comparison between the non-unity Lewis (blue) and unity Lewis modeling approach (red). In addition, the PDF of curvature (a) and strain rate (b) for both unity and non-unity Lewis number modeling approach are depicted. Note that the double peak behavior, seen in (b) for non-unity Lewis number approach, is attributed to the evaluation plane of the flame leading finger. The peak behavior vanishes if the entire flame front at $c = 0.7$ is analyzed instead as shown in the appendix.

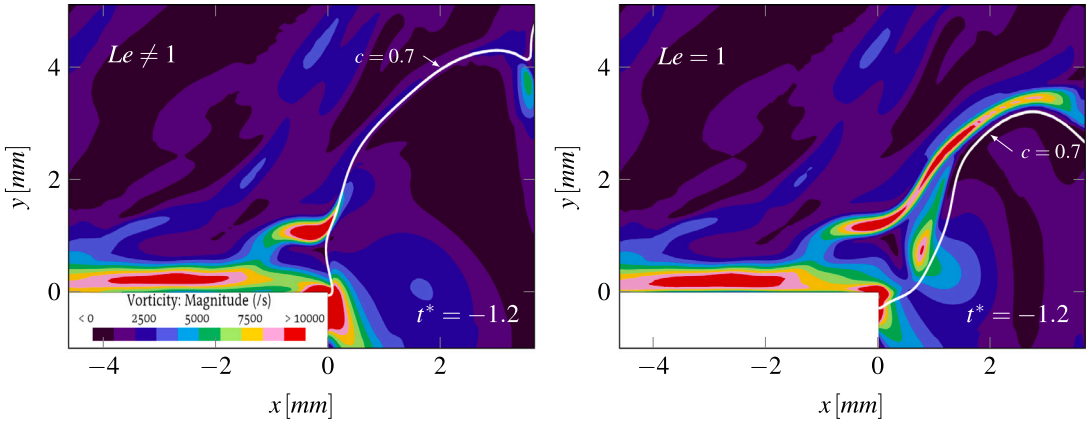

(a) Sub-unity Lewis (b) Unity Lewis

Fig. 21. Vorticity fields for sub-unity (a) and unity Lewis number approach (b). The flame front is denoted by a white isoline at $c = 0.7$. The flame in the low Lewis number flow enters the mixing tube, while the flame in the unity-Lewis number flow remains outside of the tube.

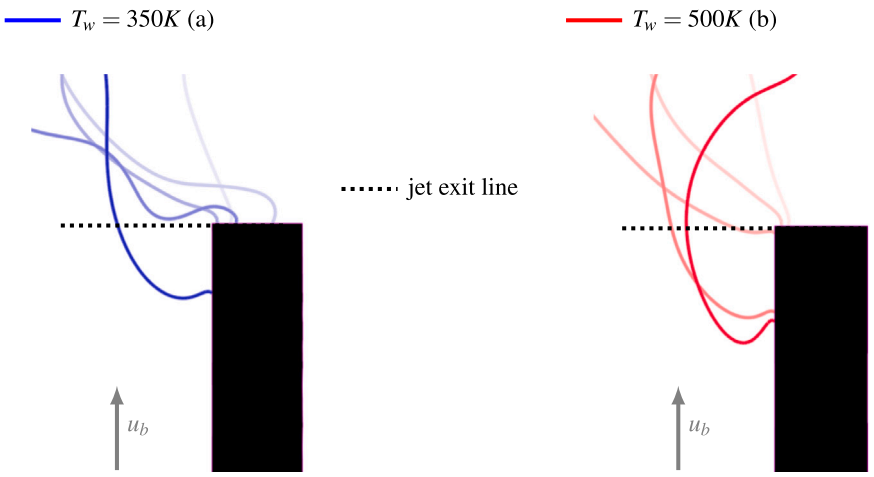

Fig. 22. Transition process for both $T_w = 350\,\mathrm{K}$ (blue) and $T_w = 500\,\mathrm{K}$ (red). Time advances with increasing opacity. Dotted black line indicate sampling line at the jet exit.

decrease of Φ or the normalized temperature reaching negative values. Note that the negative vertical axis is not shown. As soon as the values are larger than the wall temperature, this indicates flashback: second plot for the hot case, while FB becomes visible in third plot for the cold case. The transition of flashback from unconfined to a confined state occurs during the first two plots for the hot case. Since the formation of the flame finger has not yet taken place in the first plot, the curves for Φ are similar. This may be related to the opposite ejection event. The temperature and velocity are also unaffected, whereas in the cold case, the temperature increases and the velocity decreases at $r = 0.03$. This behavior is analyzed in Section 6.2 and corresponds to the ejection event. Both cases show a significant change in velocity and temperature between the first and second plot. The significant change enables flashback. In addition, the equivalence ratio increases as the wall temperature increases (Fig. 23b).

The last two diagrams are all in the state that the flame is already in the mixing tube.

We summarize that the two flashback processes are very similar. However, the hot case enters the mixing tube earlier and predicts a reduced quenching distance, as demonstrated in the simulations. The difference of $\Delta u = 3\,\mathrm{m/s}$ in the bulk velocity highlights the relevance of the wall temperature on the FB behavior.

8. Conclusion

We investigate the boundary layer flashback process of a turbulent jet-stabilized bunsen burner flame operating at pure hydrogen using well-resolved LES. Similar to the experiments, flashback occurs in regions of low velocity. Moreover, we identified quasi-coherent structures, namely low velocity streaks, in the boundary layer of the mixing tube, which are capable of transporting slow-flowing, preheated and H_2-enriched fluid outwards. This mechanism refers to an ejection event and acts as the triggering event for flame flashback. Due to heating process of the wall, the unburnt mixture is preheated close to the wall and, in addition, the equivalence ratio increases towards the wall by the Soret effect. The ejection event approaches the flame front, which in turn, responds with increased H_2-specific characteristics: the flame front is more bended towards the unburnt mixture, which is equivalent to a rise in curvature. Hence, the flame area increases significantly, leading to an enhanced turbulent flame speed. This causes the flame to move upstream towards the jet exit of the mixing tube until the flame is perpendicular to the direction of the flow. From this position, the flame propagates in the boundary layer of the mixing tube. In the following, a recirculation zone ahead of the flame is formed which facilitates the upstream propagation. Note that during the transition from unconfined to confined boundary layer flashback the flame and flow interact, which forces the positive velocity gradient over an inflection point to a negative velocity gradient in the confined state. This behavior is explained by an increased adverse pressure gradient through the flame.

We modified governing parameters in the flashback process. First, the non-unity Lewis number is replaced by an unity-Lewis number approach. There, the flame remains outside the mixing tube, which confirms, that the flashback process is clearly driven by thermo-diffusive instabilities. Second, the wall temperature is increased from $T_w = 300\,\mathrm{K}$ to $T_w = 500\,\mathrm{K}$, leading to a faster flame propagation and smaller quenching distances, which provoke flame flashback.

CRediT authorship contribution statement

P. Porath: Writing – original draft, Visualization, Validation, Software, Project administration, Methodology, Investigation, Formal analysis, Conceptualization. **L.A. Altenburg:** Writing – original draft. **S.A. Klein:** Writing – original draft. **M.J. Tummers:** Writing – original draft. **A. Ghani:** Writing – original draft, Validation, Supervision, Project administration, Methodology, Investigation, Funding acquisition, Conceptualization.

Declaration of competing interest

The authors declare that they have no known competing financial interests or personal relationships that could have appeared to influence the work reported in this paper.

Acknowledgments

This research was supported by AG Turbo and was partially funded by the BMWK under the grant number 03EE5159B. The authors would like to thank Dr. Lukasz Panek from Simens Energy for his valuable contributions and support throughout this work. We also appreciate the constructive feedback provided by the anonymous reviewers, which helped to improve the quality of this manuscript.

Appendix A. Supplementary data

Supplementary material related to this article can be found online at https://doi.org/10.1016/j.combustflame.2025.114236.

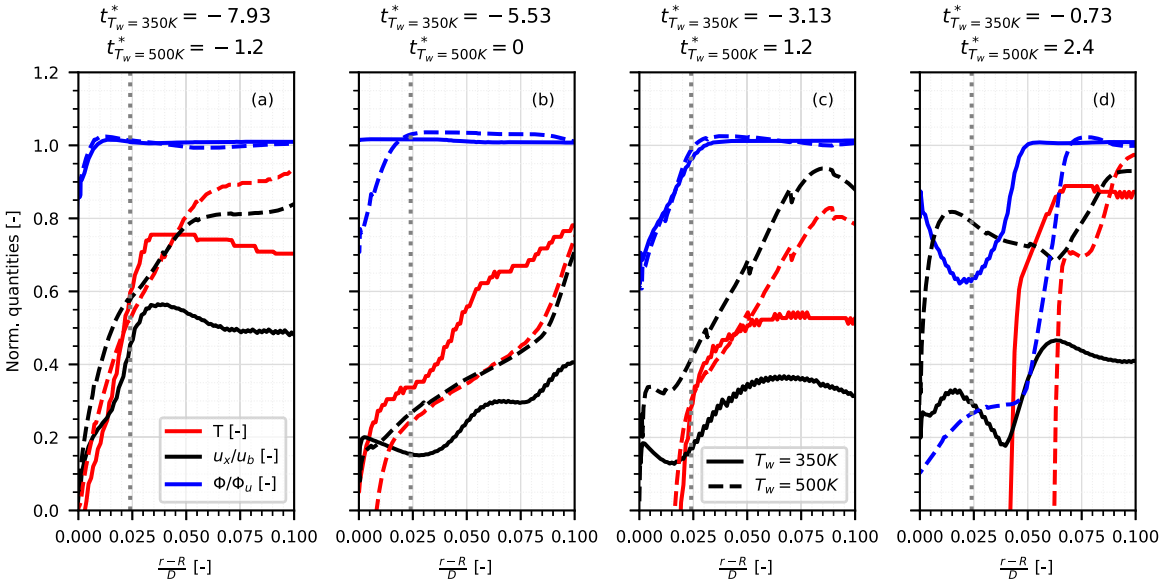

Fig. 23. Differences in axial velocity (black), temperature (red) and equivalence ratio (blue) between wall temperature of $T_w = 350\,\mathrm{K}$ (solid) and $T_w = 500\,\mathrm{K}$ (dashed) at the jet exit line, intersecting the FLP plane. Note that the time interval between the plots differ dependent on the wall temperature: for $T_w = 350\,\mathrm{K}$ is corresponds to $\Delta t = 1\,\mathrm{ms}$, while the time difference between the plots for the hotter wall temperature is $\Delta t = 0.5\,\mathrm{ms}$. This means that the FB process for hotter wall temperatures is significantly faster than observed for the colder case.

References

[1] B. Witzel, D. Moëll, N. Parsania, E. Yilmaz, M. Koenig, Development of a fuel flexible H2-natural gas gas turbine combustion technology platform, in: Turbo Expo: Power for Land, Sea, and Air, Vol. 86007, 2022, pp. 1–12.

[2] P. Clavin, Dynamic behavior of premixed flame fronts in laminar and turbulent flows, Prog. Energy Combust. Sci. 11 (1) (1985) 1–59.

[3] C. Eichler, G. Baumgartner, T. Sattelmayer, Experimental investigation of turbulent boundary layer flashback limits for premixed hydrogen-air flames confined in ducts, J. Eng. Gas Turbine Power (2012) 1–8.

[4] Y.-C. Lin, S. Daniele, P. Jansohn, K. Boulouchos, Turbulent flame speed as an indicator for flashback propensity of hydrogen-rich fuel gases, J. Eng. Gas Turbine Power 135 (11) (2013) 1–8.

[5] G. Baumgartner, L.R. Boeck, T. Sattelmayer, Experimental investigation of the transition mechanism from stable flame to flashback in a generic premixed combustion system with high-speed micro-particle image velocimetry and Micro-PLIF combined with chemiluminescence imaging, J. Eng. Gas Turbine Power 138 (2) (2016) 1–10.

[6] A. Goldmann, F. Dinkelacker, Experimental investigation and modeling of boundary layer flashback for non-swirling premixed hydrogen/ammonia/air flames, Combust. Flame 226 (2021) 362–379.

[7] F. Faldella, S. Eisenring, T. Kim, U. Doll, P. Jansohn, Turbulent flame speed and flame characteristics of lean premixed H2-CH4 flames at moderate pressure levels, J. Eng. Gas Turbine Power 146 (2) (2024).

[8] A. Gruber, J.H. Chen, D. Valiev, C.K. Law, Direct numerical simulation of premixed flame boundary layer flashback in turbulent channel flow, J. Fluid Mech. 709 (2012) 516–542, http://dx.doi.org/10.1017/jfm.2012.345.

[9] A. Endres, Numerical Modelling of Boundary Layer Flashback in Premixed Hydrogen-Air Combustion Systems (Ph.D. thesis), TU München, 2020.

[10] G. Chen, H. Wang, A. Gruber, K. Luo, J. Fan, Study of flame–flow interactions in turbulent boundary layer premixed flame flashback over a flat plate using direct numerical simulation, J. Fluid Mech. 971 (2023) 1–26.

[11] C. Jiménez, D. Fernández-Galisteo, V.N. Kurdyumov, DNS study of the propagation and flashback conditions of lean hydrogen-air flames in narrow channels: Symmetric and non-symmetric solutions, Int. J. Hydrog. Energy 40 (36) (2015) 12541–12549.

[12] A.G. Novoselov, D. Ebi, N. Noiray, Confined boundary-layer flashback flame dynamics in a turbulent swirling flow, AIAA J. 61 (4) (2023) 1548–1554.

[13] A. Kalantari, V. McDonell, Boundary layer flashback of non-swirling premixed flames: Mechanisms, fundamental research, and recent advances, Prog. Energy Combust. Sci. 61 (2017) 249–292.

[14] C. Altantzis, C. Frouzakis, A. Tomboulides, M. Matalon, K. Boulouchos, Hydrodynamic and thermodiffusive instability effects on the evolution of laminar planar lean premixed hydrogen flames, J. Fluid Mech. 700 (2012) 329–361.

[15] F. Fruzza, H. Chu, R. Lamioni, T. Grenga, C. Galletti, H. Pitsch, The importance of Soret effect, preferential diffusion, and conjugate heat transfer for flashback limits of hydrogen-fueled perforated burners, Proc. Combust. Inst. 40 (1–4) (2024) 105581.

[16] Z. Duan, B. Shaffer, V. McDonell, Study of fuel composition, burner material, and tip temperature effects on flashback of enclosed jet flame, J. Eng. Gas Turbine Power 135 (12) (2013) 1–10.

[17] A. Gruber, R. Sankaran, E.R. Hawkes, J. Chen, Turbulent flame–wall interaction: a direct numerical simulation study, J. Fluid Mech. 658 (2010) 5–32.

[18] Z. Zhu, H. Wang, G. Chen, K. Luo, J. Fan, Interactions of turbulence and flame during turbulent boundary layer premixed flame flashback under isothermal and adiabatic wall conditions using direct numerical simulation, Phys. Fluids 35 (12) (2023).

[19] G. Bruneaux, K. Akselvoll, T. Poinsot, J. Ferziger, Flame-wall interaction simulation in a turbulent channel flow, Combust. Flame 107 (1–2) (1996) 27–44.

[20] A. Ghani, M. Miguel-Brebion, L. Selle, F. Duchaine, T. Poinsot, Effect of wall heat transfer on screech in a turbulent premixed combustor, in: Center for Turbulence Research Proceedings of the Summer Program, 2016, pp. 133–141.

[21] O. Kaplan, P. Jordan, A.V. Cavalieri, G.A. Brès, Nozzle dynamics and wavepackets in turbulent jets, J. Fluid Mech. 923 (2021) A22.

[22] P.A. Nogueira, A.V. Cavalieri, P. Jordan, V. Jaunet, Large-scale streaky structures in turbulent jets, J. Fluid Mech. 873 (2019) 211–237.

[23] E. Pickering, G. Rigas, P.A. Nogueira, A.V. Cavalieri, O.T. Schmidt, T. Colonius, Lift-up, Kelvin–Helmholtz and Orr mechanisms in turbulent jets, J. Fluid Mech. 896 (2020) A2.

[24] L.A. Altenburg, S.A. Klein, M.J. Tummers, Under review: Flame-induced pressure gradients in turbulent premixed natural gas-air and hydrogen-air jet flames, Combust. Flame (2024) 1–19.

[25] G. Willems, Unraveling Flashback Phenomena of Turbulent premixed Hydrogen-Natural Gas-Air Flames (Master thesis), TU Delft, 2022.

[26] F. Faldella, Experimental Investigation of Boundary Layer Flashback in High H2 Concentration Turbulent Premixed Jet Flames (Master thesis), TU Delft, 2020.

[27] Siemens Digital Industries Software, Simcenter STAR-CCM+, version 2021.1, 2021, Siemens.

[28] F. Nicoud, F. Ducros, Subgrid-scale stress modelling based on the square of the velocity gradient tensor, Flow Turbul. Combust. 62 (3) (1999) 183–200.

[29] A.C. Hindmarsh, P.N. Brown, K.E. Grant, S.L. Lee, R. Serban, D.E. Shumaker, C.S. Woodward, SUNDIALS: Suite of nonlinear and differential/algebraic equation solvers, ACM Trans. Math. Softw. (TOMS) 31 (3) (2005) 363–396.

[30] B.E. Poling, J.M. Prausnitz, J.P. O'connell, Properties of Gases and Liquids, McGraw-Hill Education, 2001.

[31] R.J. Kee, G. Dixon-Lewis, J. Warnatz, M.E. Coltrin, J.A. Miller, A Fortran Computer Code Package for the Evaluation of Gas-Phase Multicomponent Transport Properties, Sandia National Laboratories Report SAND86-8246, Vol. 13, Citeseer, 1986, pp. 80401–81887.

[32] N. Jarrin, S. Benhamadouche, D. Laurence, R. Prosser, A synthetic-eddy-method for generating inflow conditions for large-eddy simulations, Int. J. Heat Fluid Flow 27 (4) (2006) 585–593.

[33] L. Berger, A. Attili, H. Pitsch, Synergistic interactions of thermodiffusive instabilities and turbulence in lean hydrogen flames, Combust. Flame 244 (2022) 1–20.

[34] M. Rieth, A. Gruber, J.H. Chen, The effect of pressure on lean premixed hydrogen-air flames, Combust. Flame 250 (2023) 112514.
[35] M.P. Burke, M. Chaos, Y. Ju, F.L. Dryer, S.J. Klippenstein, Comprehensive H2/O2 kinetic model for high-pressure combustion, Int. J. Chem. Kinet. 44 (7) (2012) 444–474.
[36] F. Duchaine, S. Mendez, F. Nicoud, A. Corpron, V. Moureau, T. Poinsot, Conjugate heat transfer with large eddy simulation for gas turbine components, C. R. Mec. 337 (6–7) (2009) 550–561.
[37] B. John, P. Senthilkumar, S. Sadasivan, Applied and theoretical aspects of conjugate heat transfer analysis: A review, Arch. Comput. Methods Eng. 26 (2019) 475–489.
[38] T. Poinsot, Theoretical and Numerical Combustion, RT Edwards, 2005.
[39] T. Howarth, E. Hunt, A. Aspden, Thermodiffusively-unstable lean premixed hydrogen flames: Phenomenology, empirical modelling, and thermal leading points, Combust. Flame 253 (2023) 112811.
[40] A. Attili, S. Luca, D. Denker, F. Bisetti, H. Pitsch, Turbulent flame speed and reaction layer thickening in premixed jet flames at constant Karlovitz and increasing Reynolds numbers, Proc. Combust. Inst. 38 (2) (2021) 2939–2947.
[41] L. Berger, A. Attili, H. Pitsch, Intrinsic instabilities in premixed hydrogen flames: parametric variation of pressure, equivalence ratio, and temperature. Part 2–Non-linear regime and flame speed enhancement, Combust. Flame 240 (2022) 1–16.
[42] P.E. Lapenna, G. Troiani, F. D'Alessio, F. Creta, Synergistic interplay of thermodiffusive instability and turbulence in premixed flames, Proc. Combust. Inst. 40 (1–4) (2024) 105499.
[43] M. Matalon, Intrinsic flame instabilities in premixed and nonpremixed combustion, Annu. Rev. Fluid Mech. 39 (2007) 163–191.
[44] A. Endres, T. Sattelmayer, Large Eddy simulation of confined turbulent boundary layer flashback of premixed hydrogen-air flames, Int. J. Heat Fluid Flow 72 (2018) 151–160.
[45] A. Endres, T. Sattelmayer, Numerical investigation of pressure influence on the confined turbulent boundary layer flashback process, Fluids 4 (3) (2019) 146.
[46] V. Hoferichter, C. Hirsch, T. Sattelmayer, Prediction of confined flame flashback limits using boundary layer separation theory, J. Eng. Gas Turbine Power 139 (2) (2017) 021505.
[47] A.G. Novoselov, D. Ebi, N. Noiray, Accurate prediction of confined turbulent boundary layer flashback through a critically strained flame model, J. Eng. Gas Turbine Power 144 (10) (2022) 101013.
[48] S.B. Pope, Turbulent flows, Meas. Sci. Technol. 12 (11) (2001) 2020–2021.
[49] J.M. Wallace, H. Eckelmann, R.S. Brodkey, The wall region in turbulent shear flow, J. Fluid Mech. 54 (1) (1972) 39–48.
[50] W. Willmarth, S. Lu, Structure of the Reynolds stress near the wall, J. Fluid Mech. 55 (1) (1972) 65–92.
[51] T. Zirwes, T. Häber, F. Zhang, H. Kosaka, A. Dreizler, M. Steinhausen, C. Hasse, A. Stagni, D. Trimis, R. Suntz, et al., Numerical study of quenching distances for side-wall quenching using detailed diffusion and chemistry, Flow Turbul. Combust. 106 (2021) 649–679.